MEASUREMENTS OF VIBRATIONAL RELAXATION AND DISSOCIATION OF OXYGEN WITH LASER ABSORPTION SPECTROSCOPY WITH APPLICATIONS FOR ENERGY TRANSFER IN NONEQUILIBRIUM AIR

A THESIS
SUBMITTED TO THE DEPARTMENT OF MECHANICAL ENGINEERING
AND THE COMMITTEE ON GRADUATE STUDIES
OF STANFORD UNIVERSITY
IN PARTIAL FULFILLMENT OF THE REQUIREMENTS
FOR THE DEGREE OF ENGINEER

Kyle Owen

June 2014

© 2014 by Kyle Graham Owen. All Rights Reserved.

Re-distributed by Stanford University under license with the author.

This work is licensed under a Creative Commons Attribution-Noncommercial 3.0 United States License.
http://creativecommons.org/licenses/by-nc/3.0/us/

This dissertation is online at: http://purl.stanford.edu/db014pt4918

Approved for the department.

Ronald Hanson, Adviser

Approved for the Stanford University Committee on Graduate Studies.

Patricia J. Gumport, Vice Provost Graduate Education

This signature page was generated electronically upon submission of this thesis in electronic format. An original signed hard copy of the signature page is on file in University Archives.

Abstract

The vibrational relaxation times of oxygen were measured using laser absorption spectroscopy behind incident and reflected shocks in a shock tube. The Bethe-Teller equation was used to model the vibrational relaxation, which along with the shock jump relations were used to model the gasdynamic conditions throughout the nonequilibrium relaxation process. The absorbance was modeled based on these gasdynamic conditions while adjusting the vibrational relaxation time to fit the model to the measured oxygen absorbance time-history at wavelengths 210 - 230 nm in the Schumann-Runge system. Undiluted oxygen was studied behind incident shocks at initial post-shock translational/rotational temperatures from 1000 - 3300 K and pressures from 0.05 to 0.7 atm while a mixture of 2% oxygen in argon was studied behind incident and reflected shocks at initial translational/rotational temperatures from 1000 - 4000 K and pressures from 0.2 to 1 atm. Good agreement was found with prior experimental work by White and Millikan,[1,2] Losev and Generalov,[3] and Camac,[4] though the current relaxation time data have less scatter and reduced uncertainty. The current results are also in excellent agreement with the well-known relaxation time recommendations of Millikan and White.[5]

The dissociation rate coefficient for oxygen in argon, $O_2 + Ar \rightleftharpoons O + O + Ar$, was measured using laser absorption near 216 nm in the Schumann-Runge system in a shock tube. A mixture of 2% oxygen in argon was studied behind reflected shocks at initial equilibirum temperatures from 4400 - 7900 K and pressures from 0.2 to 1 atm. The dissociation was modeled de-coupled from vibrational relaxation, as dissociation was evident only after the test gas mixture was near vibrational equilibrium.

The dissociation rate coefficient was determined by fitting the measured oxygen absorbance time-history for each experiment using temperatures based on the incident shock speed and the shock relations and adjusting the A-factor of the dissociation rate coefficient. Good agreement was found with the prior experimental work and model of Camac and Vaughan.[6] Consistent results were also obtained for measurements with constant pressure as well as increasing pressure, validating our method to account for pressure changes by including the pressure profile in the dissociation model.

Acknowledgements

I came to Stanford and the Hanson research group with some research experience but I owe a tremendous amount of gratitude to Professor Hanson for pushing me to the next level of research expertise. He helped me develop the skills to think critically and investigate my experiments down to the finest details. During my time working with Professor Hanson, his high expectations pushed me past being content with "good enough" to realize the importance of careful experimentation.

I would also like to thank the research scientists in our group. Dr. Jay Jeffries helped me advance my knowledge of lasers and spectroscopy while Dr. David Davidson was always willing to share his wisdom, for both research and life related inquiries.

One of the main reasons I came to Stanford was to work with incredibly bright students. Not only were they smart and passionate about research, but all of my fellow students in the Hanson group were also welcoming and encouraging throughout my time here. I would especially like to thank Mitchell Spearrin for mentoring me on my first project, Marcel Nations Martin for working with me on this research project, Matt Campbell for always being encouraging, and Andy Tulgestke and Luke Zaczek who started with me and shared the joys of classwork!

Throughout my graduate experience my wife has been right by my side encouraging me and making sure I'm living a balanced life, appreciating all of God's creation - not just the science behind it.

We would like to thank Professor Ibraguimova and Dr. Bykova at the Institute of Mechanics of Moscow State University for performing the absorbance model calculations using their Spectrum code. This work was supported by the Air Force

Office of Scientific Research Grant FA9550-12-1-0483 with contract monitors Dr. J. Luginsland and Dr. J. Marshall.

Contents

Abstract **v**

Acknowledgements **vii**

1 Introduction **1**

1.1 Thermochemical Nonequilibrium in High Speed Flight and Re-entry . 1

1.2 Vibrational Relaxation 1

1.2.1 Previous Measurements 4

1.2.2 Current Measurements 5

1.3 Dissociation 5

2 Absorption Model **7**

2.1 Schumann-Runge System Spectroscopy 7

2.2 Modeling UV Absorption of Molecular Oxygen 11

2.3 Absorption Model Validation 26

3 Experimental Method **30**

3.1 Experimental Setup 30

3.2 Vibrational Relaxation in a Shock Tube 32

3.3 Dissociation Model 39

4 Results **41**

4.1 Vibrational Relaxation Experiments 41

4.2 Dissociation Experiments 45

5 Summary and Future Work **50**
5.1 Summary of Current Results 50
5.2 Future Work 51

Bibliography **52**

List of Tables

2.1 Description of the term symbols for the excited and ground states of the Schumann-Runge system. 10

2.2 Effective rotational degeneracy determined by plus or minus in nuclear degeneracy term for ground and excited state based on Bose-Einstein statistics. 11

2.3 Branch symbols for six main branches. 11

2.4 Branch symbols for six satellite branches. 13

2.5 Equations used to calculate the Hönl-London factors taken from Reference.[7] The left two columns list the main branches while the right two columns list the satellite branches. The satellite branches are thus called because they have a one in the numerator and a function of J in the denominator so they diminish as J increases. 17

3.1 Oxygen/Argon dissociation reactions with the dissociation rate coefficients taken from the model by Baulch et. al.[8] 39

4.1 The measurement initial conditions and results are listed for the 2% O_2/Ar mixtures studied behind reflected shock waves (* indicates incident shocks) and the undiluted O_2 studied behind incident shock waves. 43

4.2 Values of the dissociation rate coefficient, k_d, for the dissociation reaction $O_2 + Ar \rightleftharpoons O + O + Ar$ measured for mixtures of 2% O_2 in Ar at each initial equilibrium temperature and pressure along with the dP/dt, defined here as the percent change in the pressure during the time for 99% dissociation. 48

List of Figures

1.1 The vibrational temperature describes the fractional population in each of the vibrational levels assuming a Boltzmann distribution. 2

2.1 Potential energy surfaces as a function of internuclear distance for the ground state of molecular oxygen $\left(X^3\Sigma_g^-\right)$ and the excited state $(B^3\Sigma_u^-)$ associated with the Schumann-Runge system. Adapted from a more complete energy diagram by Krupenie.[9] 8

2.2 Schematic showing examples of absorption transitions for each of the 12 branches. The even N levels in the ground state and odd N levels in the excited state are shown in grey because they are not populated due to the nuclear spin effects. The bold arrows indicate the transitions of main branches. 12

2.3 Linestrength values of the transitions for the $7 \leftarrow 4$ band from all 12 branches at an equilibrium temperature of 300 K. It can be seen that as the J value increases (moving toward longer wavelengths), the satellite branches quickly become negligible when compared to the main branches. 18

2.4 The main P and R branches are shown for transitions from $v'' = 4$ of the ground state to all vibrational levels $v' = 0-21$ of the excited state. The envelope of the maximum linestrength in each band is also shown as it is used to compare transitions from various ground vibrational levels in Figure 2.5. 19

2.5 The envelope of the maximum linestrength in each band is compared for ground state vibrational levels $v'' = 0 - 7$ at 300 K, 3000 K, and 6000 K. 20
2.6 The modeled spectral absorbance for a 2% O_2 mixture at 1 atm and an equilibrium temperature of 3000 K with a path length of 15.24 cm. The relative intensity (a.u.) of the broad laser source which has a Gaussian shape and a FWHM of 0.18 nm is overlaid on the spectral absorbance to show that the light source is broader than the absorption features. 22
2.7 The laser intensity was measured while the wavelength was scanned using a monochromator and then fit with a Gaussian profile. Over the wavelength range of interest, the FWHM of the laser was measured to be 0.18 nm. 23
2.8 Modeled cross sections in the wavelength region of interest for equilibrium temperatures of 1000, 2000, and 3000 K. 24
2.9 Absorption cross section of oxygen at 211.2 nm as a function of the vibrational temperature and equal rotational and translational temperatures. (a) shows the dependence on T_{V} and $T_{\mathrm{R}} = T_{\mathrm{T}}$, (b) shows the extreme cases from (a), illustrating the dependence on T_{V} dominates the dependence on $T_{\mathrm{R}} = T_{\mathrm{T}}$. 25
2.10 Envelope of maximum band strengths for bound-bound transitions from each lower vibrational level to all upper vibrational levels at 3000 K. The blue and red dashed lines show that measurements of the absorption near 211 nm and 223 nm are dominated by vibrational levels 4 and 5, respectively. 26
2.11 Measured absorbance at 222.95 nm and pressure for a mixture of 15% O_2, 15% He in Ar behind a reflected shock wave at an equilibrium temperature of 2431 K. 27

2.12 Comparison between the model developed in this work which only included bound-bound (b-b) transitions with the Spectrum model[10] which included both bound-bound and bound-unbound transitions. Measurements taken near 211.2 and 223.15 nm show agreement with the general trend of the models. 28
2.13 Measured oxygen absorption cross section near 223 nm at 2400 K compared to the Spectrum Model. 29

3.1 Schematic of the UV laser setup used to measure vibrational relaxation and dissociation behind incident and reflected shocks in a shock tube. 31
3.2 "x-t" diagram of an incident and reflected shock in a shock tube showing the relaxation zones. The inset shows representative translational (T_{T}), rotational (T_{R}), and vibrational (T_{V}) temperatures over time along the particle path. 34
3.3 Comparison between measured absorbance at 211.2 nm behind a reflected shock wave for a 2% O_2/Ar test gas and modeled absorbance with relaxation times from the Millikan and White correlation[5] and the scaled time to best fit the measurement. Initial (R2-F5) conditions: T_{T} = 3033 K, P = 0.46 atm, Millikan and White $\tau_{\mathrm{V\text{-}T}}$ = 11.5 μs, Best Fit $\tau_{\mathrm{V\text{-}T}}$ = 11.7 μs. 37
3.4 Comparison between measured absorbance at 223.1 nm behind an incident shock wave for an undiluted O_2 test gas and modeled absorbance with relaxation times from the Millikan and White correlation[5] and the scaled time to best fit the measurement. Initial (F2) conditions: T_{T} = 2235 K, P = 0.12 atm, Millikan and White $\tau_{\mathrm{V\text{-}T}}$ = 33.3 μs, Best Fit $\tau_{\mathrm{V\text{-}T}}$ = 32.5 μs. 38

3.5 Absorbance and pressure measurements for two sample experiments during dissociation of a mixture of 2% oxygen in argon along with the best fit modeled absorbance shown in black. (a) shows a case with a pressure rise that had an initial (vibrational-equilibrium) temperature of 6832 K and the absorbance was measured at 216 nm. (b) shows a case with near-constant pressure that had an initial (vibrational-equilibrium) temperature of 6006 K and the absorbance was measured at 215.35 nm. 40

4.1 Vibrational relaxation times plotted on a Landau-Teller diagram. The vibrational relaxation time of oxygen was measured behind incident shocks (I.S.) and reflected shocks (R.S.) for undiluted oxygen and mixtures of 2% O_2/Ar. The measurements are compared to the empirical correlation given by Equations 3.2 and 3.3 and the previous experiments used to develop the correlation. (a) shows a close view of our data demonstrating the lower scatter of our measurements compared with previous experiments. (b) shows a broader temperature range to show all the previous experiments. 42

4.2 The effects of uncertainty in the pressure, incident shock speed, time zero, laser linewidth, and best fit on the measured value of $P\tau_{\text{V-T}}$ along with the overall uncertainty. 45

4.3 Values of the dissociation rate coefficient, k_d, for the dissociation reaction $O_2 + Ar \rightleftharpoons O + O + Ar$ measured for mixtures of 2% O_2 in Ar compared to previously published models[6,8] and experiments.[6,11–14] dP/dt is defined here as the percent change in the pressure during the time for 99% dissociation. (a) shows a close view of our data demonstrating the lower scatter of our measurements compared with previous experiments. (b) shows a broader temperature range to show all the previous experiments. 47

Chapter 1: Introduction

1.1 Thermochemical Nonequilibrium in High Speed Flight and Re-entry

Recent hypersonic vehicle flight programs have successfully demonstrated high-speed flight capabilities, however the many partial successes, setbacks, and failures to meet mission objectives reveal that there is still a significant lack of understanding of the flow phenomena around and through hypersonic vehicles.[15–18] One aspect that is challenging to understand is the thermal balance around the vehicle owing to convection from the external hypersonic flow. For both hypersonic and re-entry vehicles, a strong bow shock wave develops around the vehicle. Across the shock there is a signficant temperature rise that leads to internal energy transfer and chemical reaction. The high flow speed and relatively small length scale of the nose of the vehicle lead also to conditions in which these processes do not reach equilibrium before the flow reaches the surface of the vehicle.[19] Due to this thermochemical nonequilibrium, the rates at which these processes take place must be understood in order to predict the heat transfer to the vehicle.

1.2 Vibrational Relaxation

The focus of this work will be on investigating the internal energy transfer processes that lead to thermal nonequilibrium in oxygen. Thermal nonequilibrium implies that the gas can be described by different temperatures. The temperature of a gas is

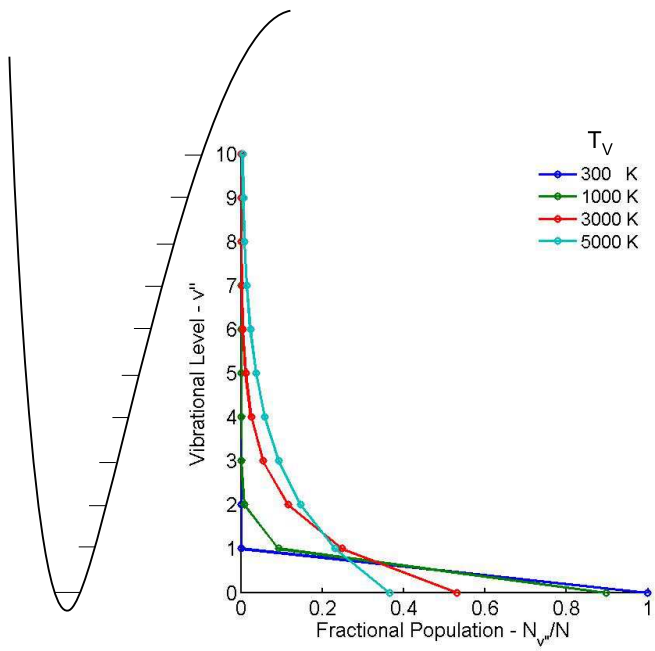

Figure 1.1: The vibrational temperature describes the fractional population in each of the vibrational levels assuming a Boltzmann distribution.

a measure of the fractional population distribution in different energy levels. Since molecules have translational, rotational, vibrational, and electronic energy, in thermal nonequilibrium these energy modes may have different temperatures. A common two-temperature model assumes that the rotational temperature equals the translational temperature and the electronic temperature equals the vibrational temperature.[20] Figure 1.1 shows how the fractional population in a given vibrational level changes with temperature for a Boltzmann distribution.

As a shock wave passes through a gas there is a sudden increase in energy, and a redistribution of populations in different quantum states. The translational energy typically arrives at a new Boltzmann distribution in the time of a few collisions.[21] On a longer time scale, collisions lead to intermolecular energy transfer including rotational-translational (R-T), vibrational-translational (V-T), and vibrational-vibrational (V-V). The process by which these collisions and hence energy transfer eventually lead to

thermal equilibrium is called relaxation. Since the rotational energy approaches equilibrium with the translational energy within several collisions,[21] the rotational temperature is generally set equal to the translational temperature in the two-temperature model. Unlike rotational energy, however, in some cases the vibrational energy takes orders of magnitude more collisions to approach equilibrium. The process by which energy is transferred to vibrational energy until the system reaches thermal equilibrium is termed vibrational relaxation.

The rate of the V-T process is often described by the Bethe-Teller (B-T) equation,[22,23] derived for an assumed harmonic oscillator model for the relaxing molecule,

$$\frac{dE_{\mathrm{V}}}{dt} = \frac{E_{\mathrm{V}}^{*}(T_{\mathrm{T}}) - E_{\mathrm{V}}(T_{\mathrm{V}})}{\tau_{\text{V-T}}(T_{\mathrm{T}})} \tag{1.1}$$

Here, E_{V}^{*} is the equilibrium energy in the vibrational mode that occurs when the vibrational temperature, T_{V}, is equal to the translational temperature, T_{T}. This equation states that the vibrational energy E_{V} will change (relax) at a rate proportional to the difference $E_{\mathrm{V}}^{*}(T_{\mathrm{T}}) - E_{\mathrm{V}}(T_{\mathrm{V}})$ until $E_{\mathrm{V}} = E_{\mathrm{V}}^{*}$, when $T_{\mathrm{V}} = T_{\mathrm{T}}$. In this B-T model, the relaxation time, $\tau_{\text{V-T}}$, is related to a microscopic rate constant $k_{1,0}$ by

$$\tau_{\text{V-T}} = \frac{1}{k_{1,0}\left[1 - \exp\left(\frac{-\theta_{\mathrm{V}}}{T_{\mathrm{T}}}\right)\right]} \tag{1.2}$$

where $k_{1,0}$ is the rate constant for collision-induced transitions from vibrational level 1 to level 0 and θ_{V} is the characteristic vibrational temperature. A detailed expression for the relaxation time based on a simplified, approximate collision model was presented by Clark and McChesney.[23]

$$p\tau_{\text{V-T}} \propto \frac{T_{\mathrm{T}}^{2/3}\left(\theta_{\mathrm{V}}L\right)^{-1/3}\tilde{m}^{-1/6}}{1 - \exp\left(\frac{-\theta_{\mathrm{V}}}{T_{\mathrm{T}}}\right)} \exp\left(C\theta_{\mathrm{V}}^{2/3}L^{2/3}\tilde{m}^{1/3}T_{\mathrm{T}}^{-1/3}\right) \tag{1.3}$$

where C, L, $\tilde{m}$, and θ_{V} are constants. The strongest temperature dependence is in the $\exp\left(T_{\mathrm{T}}^{-1/3}\right)$ term, which leads to the form seen in a Landau-Teller plot where $\ln(p\tau)$ is a linear function of $T_{\mathrm{T}}^{-1/3}$.

Derivation of the B-T equation was based on a simple harmonic oscillator (SHO). This approximation implies that all of the vibrational levels are equally spaced; quantum mechanics then yields the selection rule that limits vibrational level changes to ± 1. Also, detailed balancing and the recursion relationship from quantum mechanics lead to $k_{i,i-1} = ik_{1,0}$ and $k_{i,i-1}N_i = k_{i-1,i}N_{i-1}$, respectively, which allows the rate of vibrational energy change to be written as a function of $k_{1,0}$ as the only rate constant. Another key result of the SHO model is that a distribution will evolve thorugh a sequence of Boltzmann distributions during relaxation, i.e. T_{V} will always be defined. Since real molecules are anharmonic oscillators (AHO), these relationships are not exact but are widely used in the literature and for interpreting relaxation rate experiments. In the present analysis we have assumed that Equation 1.1 holds but that the relaxation time must be determined empirically. An interesting question is whether the current experiments, which entail monitoring absorption from excited vibrational levels, will reveal any breakdown of the B-T equation.

1.2.1 Previous Measurements

An expression similar to the form of Equation 1.3 was presented by Millikan and White,[5] chosen to fit a range of available experimental data and generally referred to as the systematics of vibrational relaxation,

$$\ln\left(p\tau_{\text{V-T}}\right) = (-18.42) + \left(1.16 \times 10^{-3}\right)\mu^{1/2}\theta_{\mathrm{V}}^{4/3}\left(T_{\mathrm{T}}^{-1/3} - (0.015)\mu^{1/4}\right) \tag{1.4}$$

Here, the units of the quantity $p\tau$ are atm-s and those of the reduced mass μ are amu (atomic mass units).

Vibrational relaxation is an important aspect of non-equilibrium gasdynamics. Previously, vibrational relaxation has been measured using shock tubes behind incident shock waves using interferometry,[1,2,21,24–27] IR emission,[25,26] and end-wall pressure measurements,[27–30] as well as behind reflected shock waves using vacuum ultraviolet (VUV) light absorption.[31] Reflected shock measurements have an advantage over incident shock measurements because high temperatures and pressures can be achieved with relatively lower driver pressures.[31] Some of these and many other

measurements were analyzed by Millikan and White to develop the semiempirical correlation between observed relaxation times and relevant molecular constants[5] shown in Equation 1.4.

Although most data for oxygen were obtained several decades ago and at temperatures below 4000 K, recently the vibrational relaxation of undiluted oxygen was measured behind incident shocks at temperatures between 6000 - 11000 K.[14] It was found that at these high temperatures the temperature dependence of $\tau_{\text{V-T}}$ deviates from the Landau-Teller relationship. In particular, the experimentally determined vibrational relaxation times were found to be longer than predicted by the Millikan and White correlation by an increasing fraction with increasing T_{T}.

1.2.2 Current Measurements

In the present work we measured the vibrational relaxation times of oxygen behind incident and reflected shock waves using laser absorption spectroscopy. Experiments were performed on mixtures of 2% oxygen in argon behind reflected shock waves with initial post-shock translational/rotational temperatures from 1000 - 4000 K and pressures from 0.2 to 1 atm and on undiluted oxygen behind incident shock waves with initial translational/rotational temperatures from 1000 - 3300 K and pressures from 0.05 to 0.7 atm.

1.3 Dissociation

The dissociation of molecular oxygen into atomic oxygen by the reaction $\mathrm{O_2} \rightleftharpoons 2\,\mathrm{O}$ dominates the formation of oxygen atoms behind the bow shock and is intimately related to the vibrational relaxation process. This plays an important role in the heat transfer process. In the present work, we measured the rate coefficient for the dissociation reaction $\mathrm{O_2} + \mathrm{Ar} \rightleftharpoons \mathrm{O} + \mathrm{O} + \mathrm{Ar}$ using laser absorption spectroscopy. Experiments were performed on mixtures of 2% oxygen in argon behind reflected shock waves with initial equilibrium temperatures from 4400 - 7900 K and pressure from 0.2 to 1 atm. Previous models have been developed that include rates for this

reaction that differ by a factor of 2 over this temperature range[6,8] as well as previous experiments[6,11–14] with results scattered near the rates predicted by the models. The present work demonstrates the capability of modern laser absorption spectroscopy to accurately study the thermochemical nonequilibrium processes that take place in hypersonic vehicles in addition to contributing lower scatter measurements of this reaction.

Chapter 2: Absorption Model

2.1 Schumann-Runge System Spectroscopy

Molecules absorb energy in discrete amounts corresponding to their possible energy levels. When light interacts with a medium the photons can either be reflected, absorbed, or transmitted. When a photon of light at a particular frequency, ν, with energy corresponding to the difference in two energy levels interacts with a molecule, the molecule may absorb this photon and be excited to a higher energy state.

A laser at a wavelength corresponding to this frequency/energy when passing through this gas will, therefore, have lower transmitted intensity then it would if the gas were not present. This phenomenon is described by Beer's Law,

$$\tau_\nu = \frac{I}{I_o} = \exp\left(-k_\nu L\right) \tag{2.1}$$

where the transmissivity, τ_ν, is the fraction of laser intensity that is transmitted through the medium when the spectral absorption coefficient of the gas is k_ν (cm^{-1}) and the path length of the laser through the absorbing gas is L (cm). The term in the exponential is also called the spectral absorbance, α_ν. Strictly speaking, this relationship is only applicable to monochromatic light.

In order to quantitatively measure properties of oxygen with absorption spectroscopy, the absorption must be modeled accurately. Oxygen absorbs most strongly in the UV due to the Schumann-Runge $\left(B^3\Sigma_u^- \leftarrow X^3\Sigma_g^-\right)$ system. The Herzberg I $\left(A^3\Sigma_u^+ \leftarrow X^3\Sigma_g^-\right)$, II $\left(c^1\Sigma_u^- \leftarrow X^3\Sigma_g^-\right)$, and III $\left(A'^3\Delta_u \leftarrow X^3\Sigma_g^-\right)$ systems overlap with the Schumann-Runge system for wavelengths longer than 240 nm,[9] however

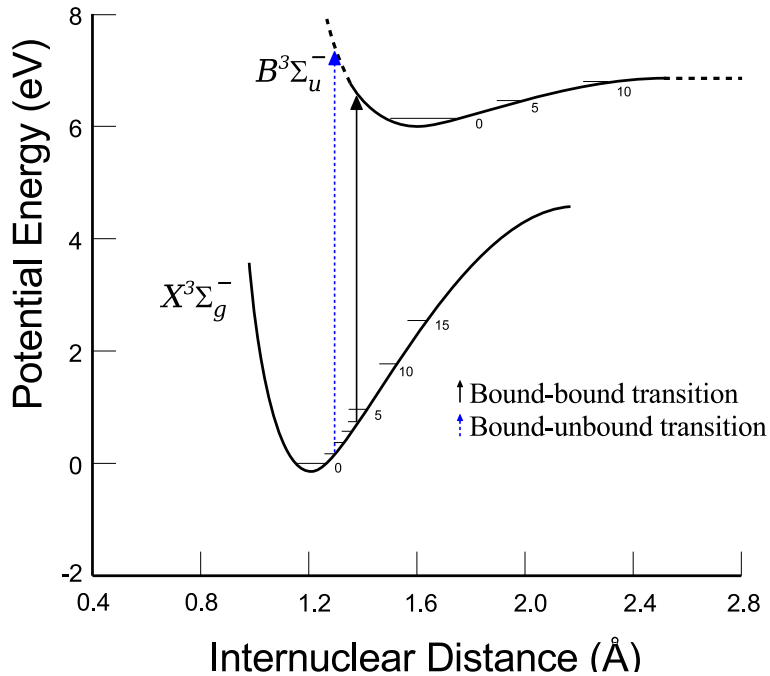

Figure 2.1: Potential energy surfaces as a function of internuclear distance for the ground state of molecular oxygen $\left(X^3\Sigma_g^-\right)$ and the excited state $(B^3\Sigma_u^-)$ associated with the Schumann-Runge system. Adapted from a more complete energy diagram by Krupenie.[9]

the Schumann-Runge system is the main contribution to the absorbance of UV light between 130 – 270 nm.[10] Therefore, only the Schumann-Runge system was modeled.

Figure 2.1 shows the potential energy surfaces for the ground state of oxygen and the excited state of the Schumann-Runge system. Since the excited state is shifted towards longer internuclear distances, transitions to the repulsive branch of the potential curve are bound-unbound transitions which make up the Schumann-Runge continuum. This continuum is strongest at shorter wavelengths and dominates the bound-bound transitions which make up the Schumann-Runge bands below 190 nm. For wavelengths longer than 190 nm, the bands become significant and the ratio of the bands to the continuum depend on the temperature and wavelength.[10] The absorption model developed here included only the bound-bound transitions, therefore,

for the final analysis of our measurements we obtained absorption calculations for our test conditions using the "Spectrum" model that includes both bound-bound and bound-unbound transitions developed by Bykova and Kuznetsova[10] through private communication with the authors.

A detailed theoretical analysis of the spectroscopy can be found in Herzberg's volume on the spectra of diatomic molecules.[32] Here, a summary of the relevant spectroscopy will be given as it pertains to the development of the absorption model. The Schumann-Runge system involves rovibronic transitions, meaning the transition is from a lower electronic state in a specific vibrational and rotational level to a higher electronic state in a specific vibrational and rotational level. The term symbol for each of the electronic states, of the form ${}^{2S+1}\Lambda_{\Omega}$, gives information about each state and what transitions are quantum mechanically more probable. $\vec{S}$ is the total electronic spin angular momentum, $\vec{\Lambda}$ is the projection of orbital angular momentum on the internuclear axis, and $\vec{\Omega}$ is the sum of projections along the internuclear axis of electron spin and orbital angular momentum, but is only defined when $\Lambda \neq 0$. Table 2.1 lists the values of the spin and orbital angular momentum, symmetry conditions, and molecular models derived from the term symbols for the excited and ground states of the Schumann-Runge system.

The Hund's Case b model applies when $\Lambda = 0$ and $S \neq 0$, and therefore applies to both the ground and excited states. This model is characterized by the total angular momentum, $\vec{J}$, which is the sum of the angular momentum of the nuclei, $\vec{N}$, and the electron spin angular momentum, $\vec{S}$. The allowed J are $J = N+S, N+S-1, ..., N-S$ and $J \geq 0$. Since $S = 1$ there are three J's for each N, except for $N = 0$ where only spin is active and $J = 1$. The rotational energy is therefore a function of both J and N, typically written as $F_1(N)$ where $J = N + 1$, $F_2(N)$ where $J = N$, and $F_3(N)$ where $J = N - 1$. Selection rules from quantum mechanics restrict transitions to $\Delta N = \pm 1$ and $\Delta J = 0, \pm 1$ except $J' = 0 \leftarrow J'' = 0$ is forbidden. Here and throughout, a single prime indicates the upper state while a double prime indicates the lower state.

The effects of nuclear spin must also be taken into account since oxygen is a homonuclear diatomic and the symmetric placement of equivalent nuclei leads to

Table 2.1: Description of the term symbols for the excited and ground states of the Schumann-Runge system.

Excited State $\boldsymbol{B^3\Sigma_u^-}$	**Ground State** $\boldsymbol{X^3\Sigma_g^-}$
$S = 1$	$S = 1$
$\Lambda = 0$	$\Lambda = 0$
Plane Sym: $-$	Plane Sym: $-$
Cent Sym: u	Cent Sym: g
Hund's case b	Hund's case b

an effective rotational degeneracy, $g_{\text{rot,eff}}$, that is sometimes zero due to the nuclear degeneracy, g_{nuc}.

$$g_{\text{rot,eff}} = g_{\text{rot}} g_{\text{nuc}} = (2J+1)\,\frac{1}{2}\left[(2I+1)^2 \pm (2I+1)\right] \tag{2.2}$$

Since ^{16}O has nuclear spin $I = 0$

$$g_{\text{rot,eff}} = (2J+1)\,\frac{1}{2}\left[1 \pm 1\right] \tag{2.3}$$

and Bose-Einstein statistics apply. The plus or minus depends on the symmetry and the angular momentum of the nuclei, Table 2.2 lists selection criteria for Bose-Einstein statistics and shows that only odd N are populated in the ground state and only even N are populated in the excited state. This is in agreement with the selection rule which requires that $\Delta N = \pm 1$.

There are 12 allowed branches in this system. The branch symbols are written as $^{\Delta N}\Delta J_{F'F''}$. P, Q, and R represent changes of -1, 0, and $+1$ respectively. Of the 12 branches, there are six main branches listed in Table 2.3 and six satellite

Table 2.2: Effective rotational degeneracy determined by plus or minus in nuclear degeneracy term for ground and excited state based on Bose-Einstein statistics.

	Symmetry Configuration	**N**	**±**	$\boldsymbol{g}_{\text{rot,eff}}$
Ground	Σ_g^-	Odd	+	$2J+1$
		Even	-	0
Excited	Σ_u^-	Odd	-	0
		Even	+	$2J+1$

Table 2.3: Branch symbols for six main branches.

${}^{\Delta N}\Delta J_{F'F''}$	${}^{P}P_{11} = P_1$	P_2	P_3	R_1	R_2	R_3
$\Delta N = \Delta J$	–1	–1	–1	+1	+1	+1
$F'F''$	$F_1' \leftarrow F_1''$	$F_2' \leftarrow F_2''$	$F_3' \leftarrow F_3''$	$F_1' \leftarrow F_1''$	$F_2' \leftarrow F_2''$	$F_3' \leftarrow F_3''$

branches listed in Table 2.4. The main branches are more probable and therefore have a stronger absorbance, as will be described in the next section. Figure 2.2 shows a schematic of the transitions described by these 12 branches.

2.2 Modeling UV Absorption of Molecular Oxygen

The laser used in this experiment has a linewidth which is larger than the linewidth of the absorption features, therefore the spectral absorbance must be modeled first and then convoluted with the linewidth of the laser used in the experiment. The spectral

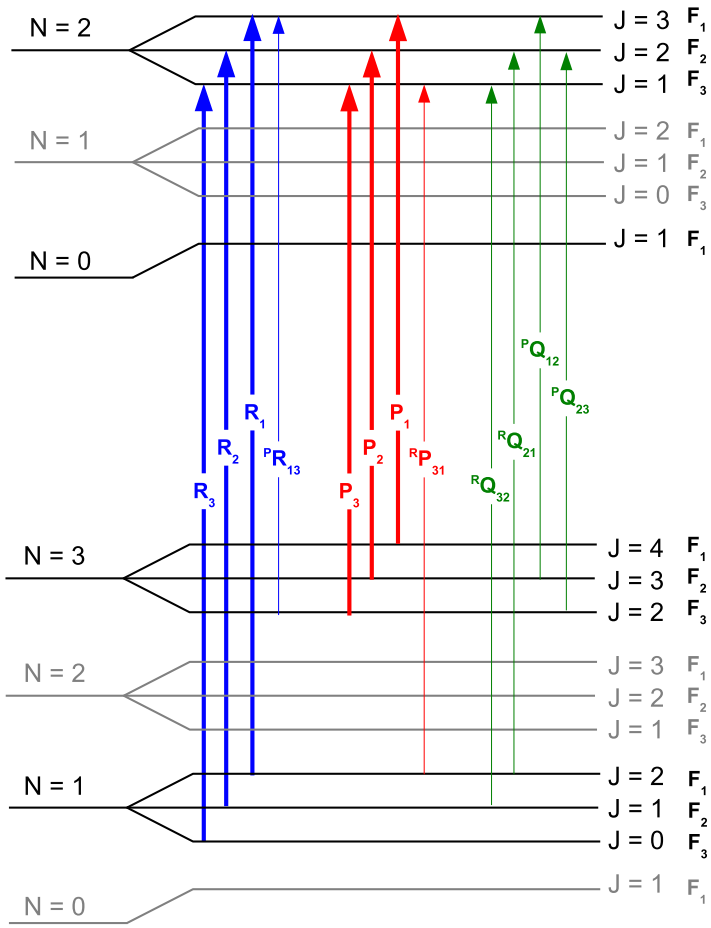

Figure 2.2: Schematic showing examples of absorption transitions for each of the 12 branches. The even N levels in the ground state and odd N levels in the excited state are shown in grey because they are not populated due to the nuclear spin effects. The bold arrows indicate the transitions of main branches.

Table 2.4: Branch symbols for six satellite branches.

$^{\Delta N}\Delta J_{F'F''}$	$^{P}R_{13}$	$^{R}P_{31}$	$^{R}Q_{21}$	$^{R}Q_{32}$	$^{P}Q_{12}$	$^{P}Q_{23}$
ΔN	–1	+1	+1	+1	–1	–1
ΔJ	+1	–1	0	0	0	0
$F'F''$	$F'_1 \leftarrow F''_3$	$F'_3 \leftarrow F''_1$	$F'_2 \leftarrow F''_1$	$F'_3 \leftarrow F''_2$	$F'_1 \leftarrow F''_2$	$F'_2 \leftarrow F''_3$

absorbance is defined as

$$\alpha_{\overline{\nu}} = -\ln\left(\frac{I}{I_o}\right) = PX_{O_2}L\sum_i S_i\phi_{i,\overline{\nu}} \tag{2.4}$$

where P (atm) is the pressure, X_{O_2} is the mole fraction of oxygen, L (cm) is the path length, S (cm^{-2}/atm) is the linestrength, ϕ_ν (cm) is the normalized lineshape function at frequency ν, and the sum is over all possible transitions. This is an important equation because, since I and I_o are measured experimentally, the gas properties can be determined by comparing the measured absorbance of oxygen to the modeled absorbance. The model for the spectral absorbance consists of determining the linecenter wavelength of each energy transition, the linestrength of the transition, and the broadening of the line. The model developed here is based on the model previously developed in Reference.[33]

The linecenter wavelength of each transition is determined from the difference in energy between the upper and lower states involved in the transition. Planck's Law relates the energy of a photon associated with a molecular transition to the frequency and wavelength of the corresponding electromagnetic wave.

$$\Delta E = E' - E'' = h\nu = \frac{hc}{\lambda} = hc\overline{\nu} \tag{2.5}$$

where Planck's constant is $h = 6.63 \times 10^{-34}$ J·sec, ν is the frequency, c is the speed

of light, λ is the wavelength, and $\overline{\nu}$ is the wavenumber. Since the energy, frequency, wavelength, and wavenumber are all related by constants, only one of these terms needs to be defined. In the following discussion the terms are used interchangeably and the constants are implied. Since spectroscopic constants are often given in terms of wavenumbers, that will be the preferred term with units of cm^{-1}. Therefore, the linecenter location of a given transition is simply the difference in energy between the upper and lower transition.

$$\overline{\nu}_o = E'(n', v', N') - E''(n'', v'', N'') \tag{2.6}$$

The relative energy of each level, therefore, must be determined. Within each electronic state there are multiple vibrational levels which each have rotational levels, so the energy of a given level has a rotational (F), vibrational (G), and electronic (T_e) component.

$$E(n, v, N) = T_e(n) + G(v) + F(N) \tag{2.7}$$

The rotational energy was determined from

$$F(N) = B_v N(N+1) - D_v N^2 (N+1)^2 \tag{2.8}$$

where B_v, is the vibrationally-dependent rotation constant and D_v is the centrifugal distortion. The splitting of the rotational level into F_1, F_2, and F_3 due to dependencies on J was determined from[32]

$$F_1(N) = F(N) + (2N+3)B_v - \lambda - \sqrt{(2N+3)^2 B_v^2 + \lambda^2 - 2\lambda B_v} + \gamma(N+1) \tag{2.9}$$

$$F_2(N) = F(N) \tag{2.10}$$

$$F_3(N) = F(N) - (2N-1)B_v - \lambda + \sqrt{(2N-1)^2 B_v^2 + \lambda^2 - 2\lambda B_v} - \gamma N \tag{2.11}$$

These energy differences were calculated using the above equations with the spectroscopic parameters taken from the literature. Since only the relative energy is important, the electronic energy of the ground state, $T_e(n'')$, is defined to be zero. The electronic energy of the excited electronic state, $T_e(n')$, and the parameters $G(v)$,

B_v, D_v accounting for anharmonicity, of levels $v = 0 - 21$ for both the ground and excited states were taken from Reference.[34] The splitting parameters, λ and γ, were taken from Reference,[35] where the parameters were given for the vibrational levels $v'' = 0 - 2$ of the ground state and $v' = 0 - 19$ of the excited state. For the ground state, since the parameters were the same for the first three vibrational levels, these constant values were used for all vibrational levels $v = 0 - 21$. For the excited state, the values for the vibrational levels $v = 20$ and 21 were extrapolated from the values of the lower levels.

The linestrength is a fundamental parameter of a specific energy transition. It represents the strength of this transition based on the number of molecules in the lower energy level at a given temperature and the probability that the molecules will undergo the transition to the higher energy level. The linestrength depends on the vibrational and rotational levels of the lower and upper states according to[33]

$$S = \frac{\pi e^2}{m_e c^2} \frac{N_{v''J''}}{P_{O_2}} f_{v''v'} \frac{S_{J''J'} T_{J''J'}}{2J'' + 1} \tag{2.12}$$

where e is the charge of an electron, m_e is the mass of an electron, c is the speed of light, $N_{v''J''}$ is the number density in the lower state, P_{O_2} is the partial pressure of oxygen in atmospheres, $f_{v''v'}$ is the absorption oscillator strength for the $v' \leftarrow v''$ band, $S_{J''J'}$ is the rotational linestrength also known as the Hönl-London factor, and $T_{J''J'}$ is a correction term accounting for vibration-rotation interaction which was assumed to be equal to unity.

The constants in the first term can be combined resulting in

$$\frac{\pi e^2}{m_e c^2} = 8.82 \times 10^{-13} (\text{cm}) \tag{2.13}$$

The second term can be rewritten as

$$\frac{N_{v''J''}}{P_{O_2}} = \frac{F_{v''J''}}{k_B T_{\text{T}}} \times 1.01325 \times 10^6 (\text{cm}^{-3}\text{atm}^{-1}) \tag{2.14}$$

where $F_{v''J''} = {}^{N_{v''J''}}/_{N_{O_2}}$ is the fractional population in $v''J''$ given by Boltzmann

statistics, and is a function of the lower state energy levels and the rotational, T_{R}, vibrational, T_{V}, and electronic, T_{E}, temperatures.

$$F_{v''J''} = \frac{2J''+1}{Q_{\mathrm{E}}(T_{\mathrm{E}})Q_{\mathrm{V}}(T_{\mathrm{V}})Q_{\mathrm{R}}(T_{\mathrm{R}})} \exp\left\{-\frac{hc}{k_B}\left[\frac{T_e(n'')}{T_{\mathrm{E}}} + \frac{G(v'')}{T_{\mathrm{V}}} + \frac{F(N'',J'')}{T_{\mathrm{R}}}\right]\right\} \quad (2.15)$$

The partition function, Q, has a component from all three types of internal energy.

$$Q_{\mathrm{E}}(T_{\mathrm{E}}) = g_0 + g_1 \exp\left(-\frac{\theta_1}{T_{\mathrm{E}}}\right) \quad (2.16)$$

$$Q_{\mathrm{V}}(T_{\mathrm{V}}) = \frac{1}{1-\exp\left(-\frac{\theta_{\mathrm{V}}}{T_{\mathrm{V}}}\right)} \quad (2.17)$$

$$Q_{\mathrm{R}}(T_{\mathrm{R}}) = \frac{T_{\mathrm{R}}}{2\theta_{\mathrm{R}}} \quad (2.18)$$

These are functions of the respective temperature and spectroscopic parameters, where $g_0 = 3$, $g_1 = 2$, $\theta_1 = 11390$ K, $\theta_{\mathrm{V}} = 2275$ K, and $\theta_{\mathrm{R}} = 2.1$ K.

For the third term of Equation 2.12, the oscillator strength can be written as a function of the band center wavelength, $\lambda_{v''v'}$ (Å), which is derived from the energy difference between the lower and upper vibrational levels, and the Einstein A coefficient, $A_{v'v''}$ (s^{-1}), which were taken from Reference[36] for each band.

$$f_{v''v'} = \frac{\lambda^2_{v''v'}}{6.67\times10^{15}} A_{v'v''} \quad (2.19)$$

The Hönl-London factors were calculated from the equations in Table 2.5 taken from Reference.[7] From these equations, the difference between the main branches and satellite branches becomes apparent. The Hönl-London factor for the satellite branches are inversely proportional to J, so as J increases they go toward zero. Figure 2.3 shows the linestrengths of the transitions for the $7 \leftarrow 4$ band from all 12 branches. Again it can be clearly seen that the linestrengths of the satellite branches are orders of magnitude lower than the main branches, especially for higher J values. In order to save computation time, based on the above justification, only the main branches were used in the modeled absorbance.

Table 2.5: Equations used to calculate the Hönl-London factors taken from Reference.[7] The left two columns list the main branches while the right two columns list the satellite branches. The satellite branches are thus called because they have a one in the numerator and a function of J in the denominator so they diminish as J increases.

Main Branches		**Satellite Branches**	
$^{\Delta N}\Delta J_{F'F''}$	$S_{J''J'}(J=J'')$	$^{\Delta N}\Delta J_{F'F''}$	$S_{J''J'}(J=J'')$
P_1	$\frac{(J-1)(2J+1)}{(2J-1)}$	$^{P}R_{13}$	$\frac{1}{(J+1)(2J+1)(2J+3)}$
P_2	$\frac{(J-1)(J+1)}{J}$	$^{R}P_{31}$	$\frac{1}{J(2J-1)(2J+1)}$
P_3	$\frac{(J+1)(2J-1)}{(2J+1)}$	$^{P}Q_{12}$	$\frac{1}{J}$
R_1	$\frac{J(2J+3)}{(2J+1)}$	$^{P}Q_{23}$	$\frac{1}{(J+1)}$
R_2	$\frac{J(J+2)}{(J+1)}$	$^{R}Q_{21}$	$\frac{1}{(J+1)}$
R_3	$\frac{(J+2)(2J+3)}{(2J+3)}$	$^{R}Q_{32}$	$\frac{1}{J}$

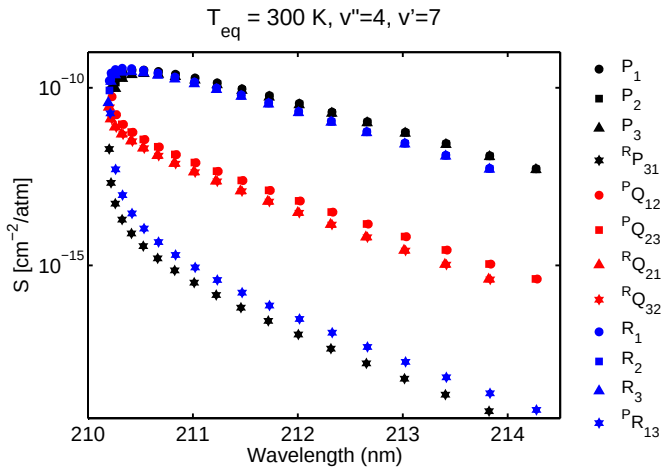

Figure 2.3: Linestrength values of the transitions for the $7 \leftarrow 4$ band from all 12 branches at an equilibrium temperature of 300 K. It can be seen that as the J value increases (moving toward longer wavelengths), the satellite branches quickly become negligible when compared to the main branches.

The entire bound-bound spectra includes transitions for all 12 branches from the allowed N'' levels in each of the ground vibrational levels to each of the excited vibrational levels. Figure 2.3 showed the linestrengths of the 12 branches for a single band. Figure 2.4 shows a comparison of linestrengths of the main branches for transitions from the same ground vibrational level to all of the excited vibrational levels. Figure 2.5 then shows an envelope of the maximum linestrengths in each band for ground vibrational levels $v'' = 0 - 7$ at equilibrium temperatures of 300 K, 3000 K, and 6000 K. It can be seen that as the temperature increases, the higher vibrational levels begin to populate and therefore the linestrengths increase.

The lineshape function is included in the spectral absorbance equation because the energy transition does not occur at a finite frequency. Due to the Heisenberg Uncertainty Principle there is uncertainty in the energy levels between which the molecule is transitioning. This leads to the absorption being distributed over a range of wavenumbers. The lineshape function describes this distribution in relative terms

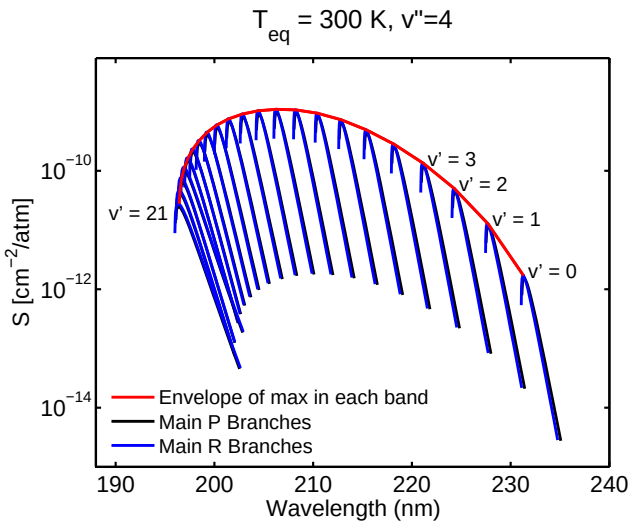

Figure 2.4: The main P and R branches are shown for transitions from $v'' = 4$ of the ground state to all vibrational levels $v' = 0 - 21$ of the excited state. The envelope of the maximum linestrength in each band is also shown as it is used to compare transitions from various ground vibrational levels in Figure 2.5.

since it is normalized to sum to one over all wavenumbers.

$$\phi \equiv \frac{k_{\overline{\nu}}}{\int k_{\overline{\nu}} d\overline{\nu}} \tag{2.20a}$$

$$\int \phi_{\overline{\nu}} d\overline{\nu} = 1 \tag{2.20b}$$

This broadening of the absorption line described by the lineshape function comes from many sources. Natural broadening based solely on the Hesienberg Uncertainty Principal is generally negligible when compared to the others. Another source of broadening is called collisional or pressure broadening. As the pressure increases the increased number of collisions between molecules leads to an increase in the uncertainty of the energy states, which in turn leads to increased broadening. In this case

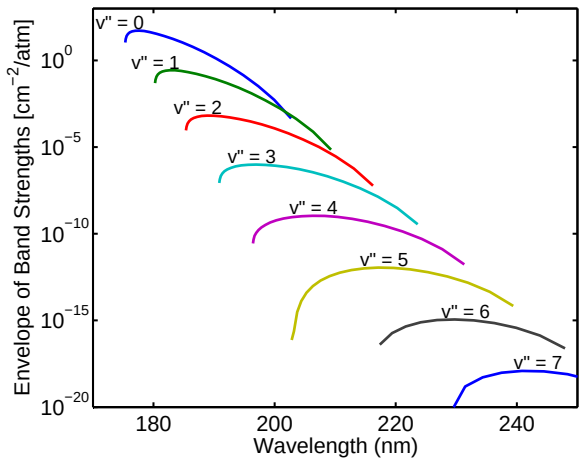

(a) T_{eq}= 300 K

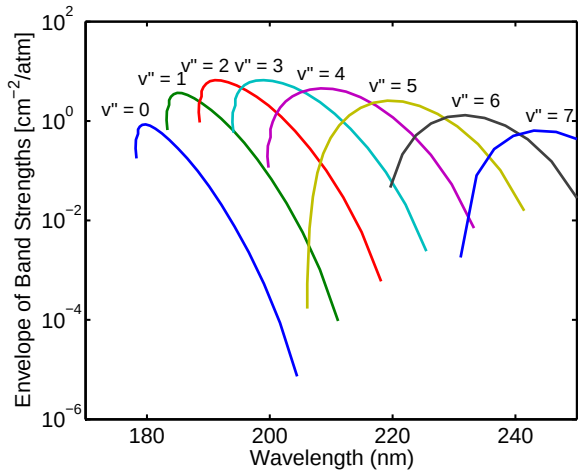

(b) T_{eq}= 3000 K

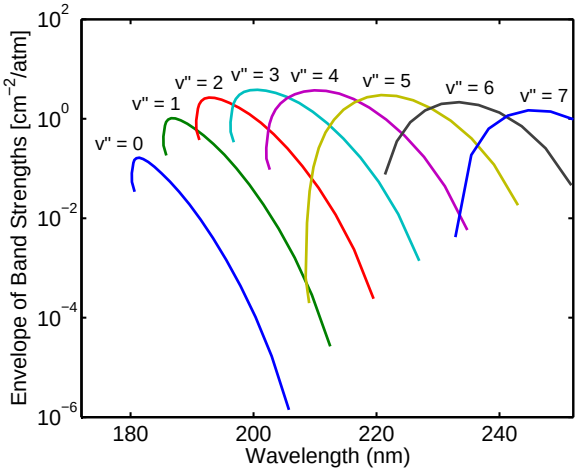

(c) T_{eq}= 6000 K

Figure 2.5: The envelope of the maximum linestrength in each band is compared for ground state vibrational levels $v'' = 0 - 7$ at 300 K, 3000 K, and 6000 K.

the lineshape function follows a Lorentzian shape.

$$\phi_c(\overline{\nu}) = \phi_c(\overline{\nu}_o)\frac{1}{1+4\left(\frac{\overline{\nu}-\overline{\nu}_o}{\Delta\overline{\nu}_c}\right)^2} \tag{2.21}$$

Where the lineshape at linecenter is

$$\phi_c(\overline{\nu}_o) = \frac{2}{\pi\Delta\overline{\nu}_c} \tag{2.22}$$

and the collisional linewidth, which is the full width at half maximum (FWHM) is generally determined experimentally. In our model we have adopted the empirical correlation described by Reference[37] based on experimental observations.

$$\Delta\overline{\nu}_c = 0.3P\left(\frac{273.2}{T_{\mathrm{T}}}\right)^{0.7} \tag{2.23}$$

Another source of broadening, called Doppler broadening, comes from the random motion of the molecules. When a molecule has a velocity component in the same direction that the laser is propagating, the frequency of the absorption shifts. Doppler broadening results from many molecules with a velocity distribution, so the lineshape function follows a Gaussian shape.

$$\phi_D(\overline{\nu}) = \phi_D(\overline{\nu}_o)\exp\left[-4\ln 2\left(\frac{\overline{\nu}-\overline{\nu}_o}{\Delta\overline{\nu}_D}\right)^2\right] \tag{2.24}$$

Where the lineshape at linecenter is

$$\phi_D(\overline{\nu}_o) = \frac{2}{\Delta\overline{\nu}_D}\left(\frac{\ln 2}{\pi}\right)^{1/2} \tag{2.25}$$

and the doppler linewidth (FWHM), is

$$\Delta\nu_D = \overline{\nu}_o(7.1623\times 10^{-7})\left(\frac{T_{\mathrm{T}}}{M}\right)^{1/2} \tag{2.26}$$

where M is the molecular weight.

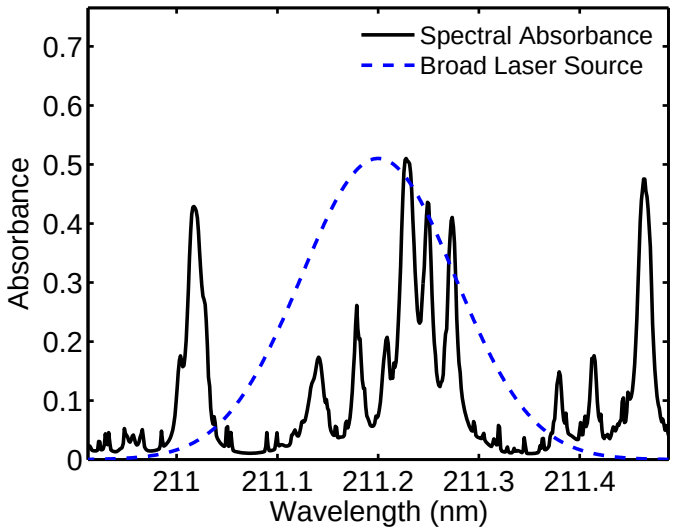

Figure 2.6: The modeled spectral absorbance for a 2% O_2 mixture at 1 atm and an equilibrium temperature of 3000 K with a path length of 15.24 cm. The relative intensity (a.u.) of the broad laser source which has a Gaussian shape and a FWHM of 0.18 nm is overlaid on the spectral absorbance to show that the light source is broader than the absorption features.

To account for both of these broadening mechanisms, the lineshapes are combined with the Voigt profile which is a convolution of the two.

$$\phi_V(\overline{\nu}) = \int_{-\infty}^{\infty} \phi_D(u)\phi_c(\overline{\nu} - u)du \tag{2.27}$$

Solutions are listed in tables and described by numerical approximations as functions of the Doppler and collisional widths.

This model enables the calculation of the spectral absorbance as a function of wavelength, mixture, pressure, path length, and temperatures (translational, rotational, vibrational, and electronic). Figure 2.6 shows the spectral absorbance near 211.2 nm at an equilibrium temperature of 3000 K. As mentioned previously, the laser has a linewidth which is larger than the linewidth of the absorption features, this can be seen by the overlaid Gaussian laser intensity profile in Figure 2.6.

To calculate the absorbance that would be measured by the broad light source

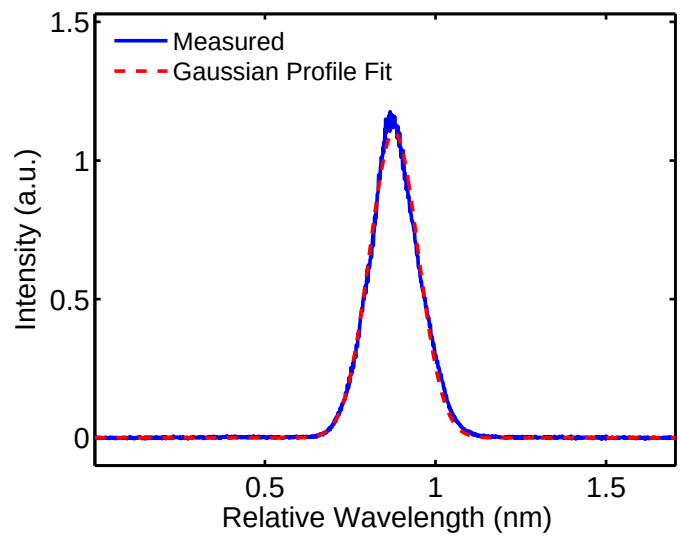

Figure 2.7: The laser intensity was measured while the wavelength was scanned using a monochromator and then fit with a Gaussian profile. Over the wavelength range of interest, the FWHM of the laser was measured to be 0.18 nm.

the signal must be degraded by an instrument function. It is necessary, therefore, to have an accurate model for the laser's intensity profile. A Spex 750M monochromator with a 1200 grooves/mm grating blazed for 150 nm was used to measure the laser intensity as a function of wavelength. Figure 2.7 shows that a Gaussian profile fit the measurd intensity satisfactorily. The FWHM of the laser was measured to be 0.18 nm, however this value has some contribution from instrument broadening so it can be interpreted as an upper bound of the laser linewidth. The Fourier transform limited linewidth was calculated[38,39] from the pulsewidth to be 0.07 nm so this can be interpreted as a lower bound of the laser linewidth. The Gaussian profile of the spectral intensity was modeled as

$$I_o(\overline{\nu}) = \frac{2}{\Delta\overline{\nu}_L}\left(\frac{\ln 2}{\pi}\right)^{1/2} \exp\left[-4\ln 2\left(\frac{\overline{\nu}-\overline{\nu}_o}{\Delta\overline{\nu}_L}\right)^2\right] \tag{2.28}$$

where $\Delta\overline{\nu}_L$ is the laser FWHM and $\overline{\nu}_o$ is the laser linecenter. For each step in the

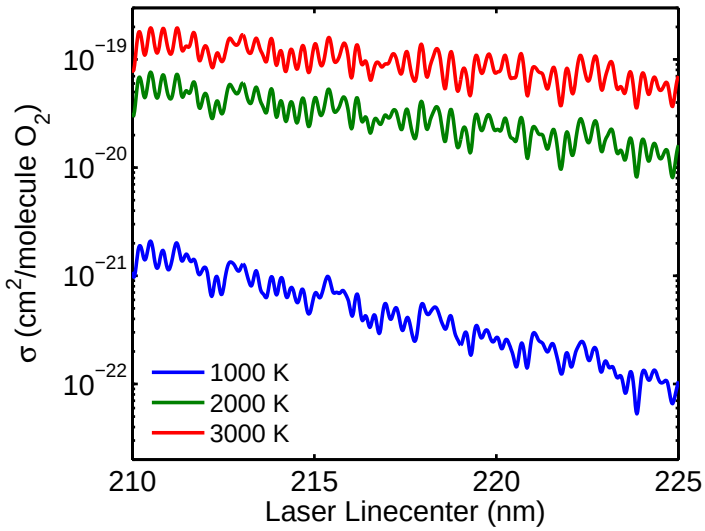

Figure 2.8: Modeled cross sections in the wavelength region of interest for equilibrium temperatures of 1000, 2000, and 3000 K.

spectral absorbance the transmitted intensity was calculated according to

$$I(\overline{\nu}) = I_o(\overline{\nu}) \exp\left(-\alpha_{\overline{\nu}}\right) \tag{2.29}$$

from which the degraded absorbance was determined as a function of the laser linecenter

$$\alpha_d(\overline{\nu}_o) = -\ln\left[\frac{\int_{\overline{\nu}_o-1.6\Delta\overline{\nu}_L}^{\overline{\nu}_o+1.6\Delta\overline{\nu}_L} I(\overline{\nu})d\overline{\nu}}{\int_{\overline{\nu}_o-1.6\Delta\overline{\nu}_L}^{\overline{\nu}_o+1.6\Delta\overline{\nu}_L} I_o(\overline{\nu})d\overline{\nu}}\right] \tag{2.30}$$

where the integration was performed numerically with a step size of 0.25 cm^{-1}.

Another way to describe the absorbance is in terms of the cross section, σ (cm^2/molecule), and the number density, n (molecules/cm^3).

$$\alpha_d = \sigma n L \tag{2.31}$$

This is helpful, because, while the absorbance depends on many parameters that are specific to a given experiment, the cross section is mainly a function of just

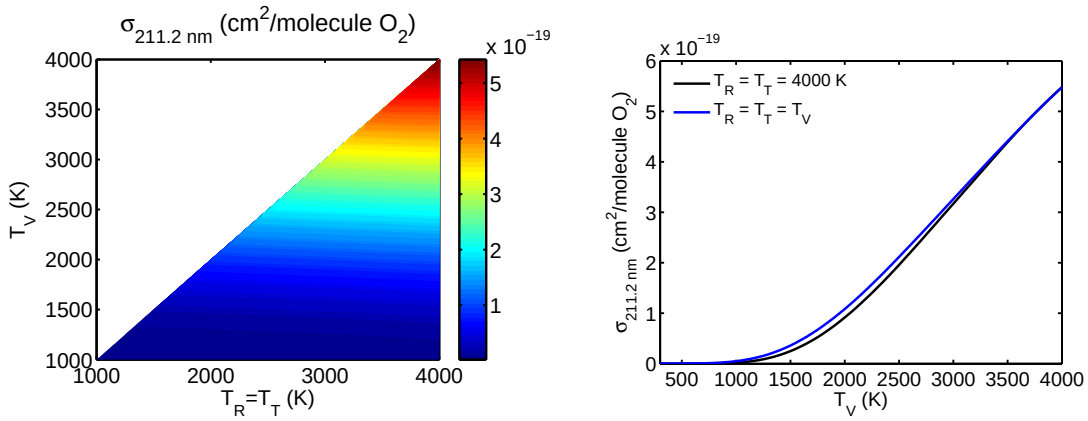

Figure 2.9: Absorption cross section of oxygen at 211.2 nm as a function of the vibrational temperature and equal rotational and translational temperatures. (a) shows the dependence on T_{V} and $T_{\mathrm{R}} = T_{\mathrm{T}}$, (b) shows the extreme cases from (a), illustrating the dependence on T_{V} dominates the dependence on $T_{\mathrm{R}} = T_{\mathrm{T}}$.

the wavelength and the temperatures. There is some pressure dependence in the cross section due to collisional broadening, but this is almost negligible since the instrument function smooths out the degraded absorbance. Figure 2.8 shows the cross section over the wavelength region of interest for equilibrium temperatures of 1000 - 3000 K. The overall trend is similar to what was seen for linestrengths in Figure 2.5, as the temperature increases the higher vibrational levels at longer wavelengths begin to populate resulting in an increase in the absorption cross section. The small fluctuations are what remains of the spectrally varying absorbance due to discrete transitions.

Since our model was developed in order to study vibrational relaxation it can be used to model nonequilibrium temperatures as well. During vibrational relaxation the rotational temperature very quickly equilibrates with the translational temperature, so this model was used to to determine the absorbance based on two temperatures, the vibrational temperature and the equilibrated rotational/translational temperature. Figure 2.9, calculated for a wavelength of 211.2 nm, shows that the cross section is significantly dependent on the vibrational temperature with only a small inverse dependence on the equilibrated rotational/translational temperature.

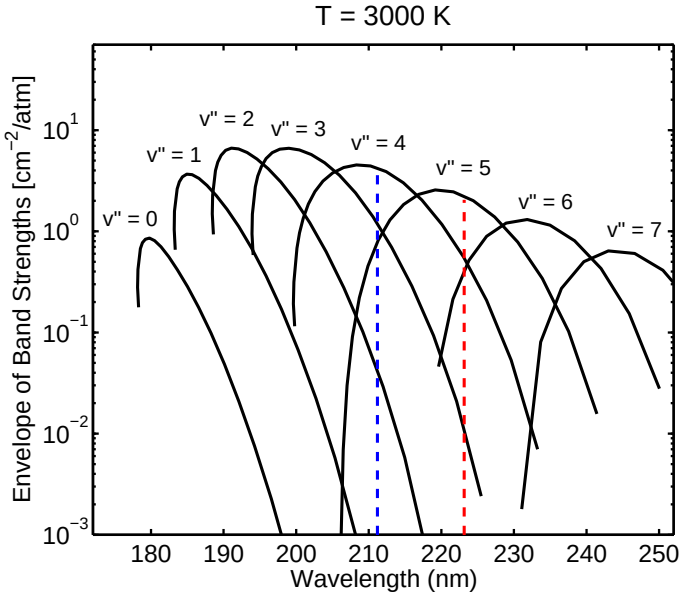

Figure 2.10: Envelope of maximum band strengths for bound-bound transitions from each lower vibrational level to all upper vibrational levels at 3000 K. The blue and red dashed lines show that measurements of the absorption near 211 nm and 223 nm are dominated by vibrational levels 4 and 5, respectively.

The strong dependence of the absorption cross section of oxygen in the Schumann-Runge system on the vibrational temperature follows from the fact that the absorption is from a specific vibrational level and the population in that level is dictated by the vibrational temperature. Figure 2.10 shows a comparison between the strengths of the transitions from different lower vibrational levels. The absorption near 211 nm and 223 nm was measured since the dominant contribution to absorption at these wavelengths is due to excitation from $v'' = 4$ and $v'' = 5$, respectively.

2.3 Absorption Model Validation

This model was developed in order to investigate the vibrational relaxation process during which the nonequilibrium temperatures are determined. Since this nonequilibrium is what is being studied, validation could not be carried out under nonequilibrium conditions, instead the model was validated by comparing the measured and

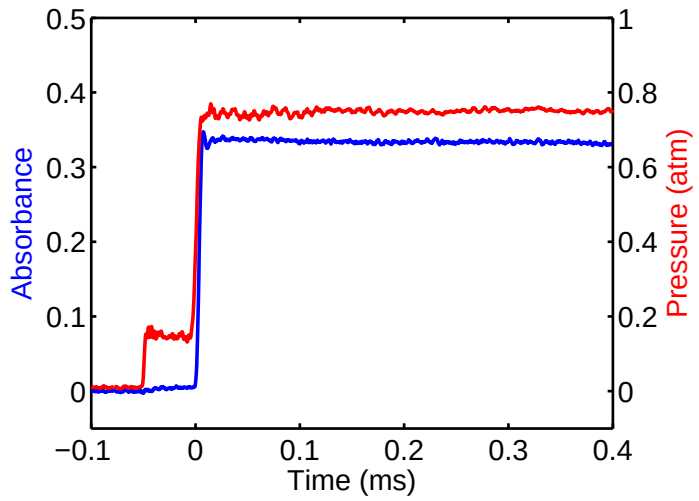

Figure 2.11: Measured absorbance at 222.95 nm and pressure for a mixture of 15% O_2, 15% He in Ar behind a reflected shock wave at an equilibrium temperature of 2431 K.

modeled cross sections after equilibrium was attained. In order to decrease the vibrational relaxation time so that equilibrium was attained faster, mixtures of 15% O_2, 15% He in Ar were studied. Figure 2.11 shows how the addition of the helium the the mixture makes the vibrational relaxation virtually instantaeous.

As mentioned previously, this model only includes the bound-bound transitions and neglects the bound-unbound transitions. Previously, the "Spectrum" model was developed by Bykova et. al.[10] that includes both types of transitions. Figure 2.12 shows a comparison between the current model for bound-bound transitions and the Spectrum model including the bound-bound component and the total which includes the bound-unbound transitions as well. The models are in good agreement at low temperatures, however they deviate as the temperature increases. The current model is lower than the bound-bound component of Spectrum, which is likely due to differences in spectroscopic parameters like the Einstein A coefficients which dictate the band strengths. The bound-unbound component of the Spectrum model increases in significance for higher temperatures and shorter wavelengths. Figure 2.12 also shows

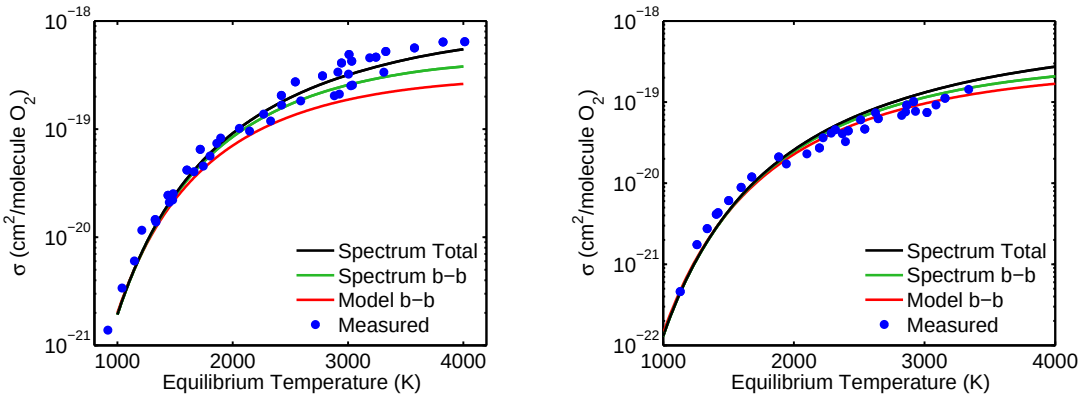

(a) $\lambda_o \sim 211.2$ nm (b) $\lambda_o \sim 223.15$ nm

Figure 2.12: Comparison between the model developed in this work which only included bound-bound (b-b) transitions with the Spectrum model[10] which included both bound-bound and bound-unbound transitions. Measurements taken near 211.2 and 223.15 nm show agreement with the general trend of the models.

our measurements of the absorption cross section as a function of equilibrium temperature at 211.2 and 223.15 nm. The measurements validate the general trend of the models, however there is too much scatter in the data to definitively validate one of the models.

The wavelength dependence of the Spectrum model was also studied by measuring the cross section at different wavelengths for the same temperature. Figure 2.13 reveals that the order of magnitude is in agreement but the wavelength dependence is not. These measurements indicate that a change in 0.1 nm can change the cross section by more than a factor of 2. This strong wavelength dependence explains some of the scatter in the measurements shown in Figure 2.12 since they were not all at the same exact wavelength.

Future work is planned in collaboration with the authors of the Spectrum model to refine the model based on these new measurements. For the remainder of this work, the Spectrum model was used to analyze our vibrational relaxation and dissociation measurements. Even though the magnitude of the model does not match the measurements exactly, the general trend of the temperature dependence is correct. Since the key measurement in both the vibrational relaxation and dissociation experiments

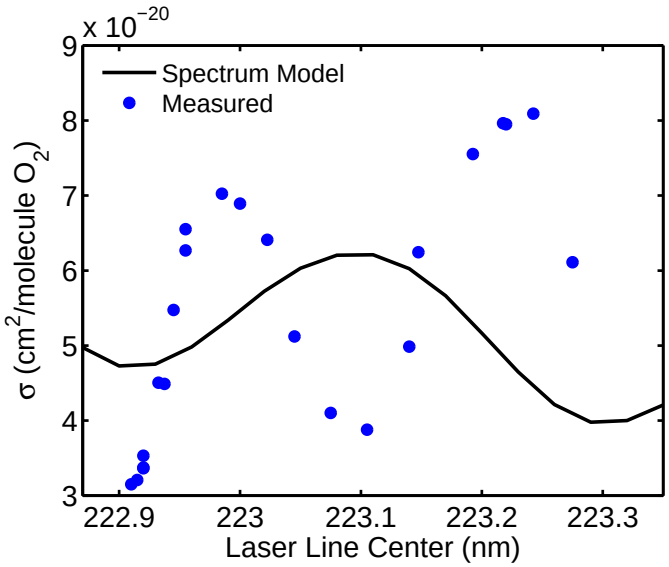

Figure 2.13: Measured oxygen absorption cross section near 223 nm at 2400 K compared to the Spectrum Model.

is the time dependence of the absorption, not the absolute magnitude, the modeled absorbance was scaled in order to match the equilibrium and initial absorbance for vibrational relaxation and dissociation measurements, respectively.

Chapter 3: Experimental Method

3.1 Experimental Setup

Laser absorption spectroscopy was used to measure the population in the vibrational levels of ground state ($X^3\Sigma$) oxygen while oxygen vibrationally relaxed and dissociated behind incident and reflected shocks.[40] Figure 3.1 shows the schematic of the laser and shock tube experimental setup, which was described in more detail previously.[41] The stainless steel shock tube has a 3.7 m driver section and a 10 m driven section with a 15.24 cm inner diameter in both sections. The incident shock velocity was measured using a series of piezoelectric pressure transducers over the last 1.5 m of the shock tube. The pressure at the measurement location was recorded using a Kistler 603B1 pressure gauge. Before each experiment, the shock tube was turbomolecular pumped to an ultimate pressure below 5×10^{-6} Torr with a leak and outgassing rate typically less than 1×10^{-5} Torr/min. A picosecond pulsed Ti:Sapphire laser (Mira HP, Coherent Inc.) was frequency quadrupled (FHG, Coherent Inc.) to generate tunable UV light between 210 – 230 nm. The fundamental output of the laser had a Gaussian spectral profile with a FWHM of ∼0.5 nm as measured by a Bristol 721 wavemeter in spectrum analyzer mode. The fourth harmonic had a Gaussian spectral profile with a FWHM between 0.07 - 0.18 nm, based on the calculated Fourier transform limit and the linewidth measured with a monochromator (Spex 750M). In these experiments, the fundamental wavelength was monitored using the Bristol wavemeter. The laser beam was focused at the center of the shock tube to a beam waist less than 0.3 mm with a 75 cm focal length lens to achieve high time resolution measurements.

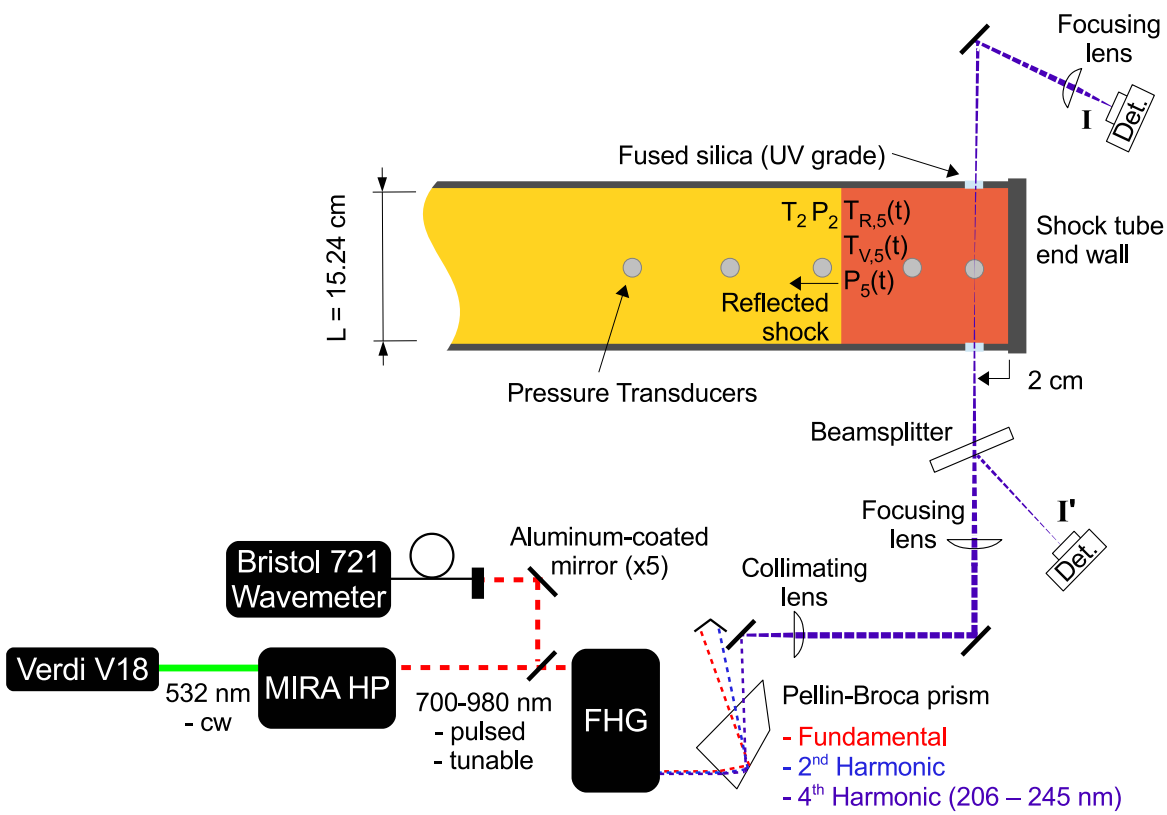

Figure 3.1: Schematic of the UV laser setup used to measure vibrational relaxation and dissociation behind incident and reflected shocks in a shock tube.

The UV beam was split with one portion going directly to a reference detector while the other passed through the shock tube through UV grade fused silica windows after which it was focused onto another detector. Reflected shock experiments were performed with the laser beam passing through the shock tube at a distance of 2 cm from the end wall. Incident shock experiments were performed with the laser in the same location, but a different end wall plug, such that the end wall was 5 cm from the measurement location in order to provide sufficient time for relaxation before the reflected shock wave arrived. The beam intensities before (I') and after (I) were measured with large area UV photoreceivers (New Focus 2032) set to a gain of 105 V/A with a bandwidth of 150 kHz. This dual-beam common-mode-rejection method effectively removed the low frequency variation in the laser intensity. The oxygen absorbance, Abs, in the vibrationally relaxing gas behind the shock was calculated using Beers Law.

$$\frac{I}{I_o} = \frac{(I/I')}{(I/I')_o} = e^{-Abs} \tag{3.1}$$

where the incident intensity, I_o, was taken as the ratio of the intensities, (I/I'), before the shock arrived as there is no absorption at room temperature and the transmitted intensity was taken as the ratio of the intensities during the relaxation and dissociation processes.

3.2 Vibrational Relaxation in a Shock Tube

Analysis of the experimental data was performed by modeling the relaxation process in the shock tube using an in-house code and comparing the model results to the experimental data for absorbance versus time. The molecule-specific empirical correlation developed by Millikan and White[5] was used as a starting point to calculate the relaxation time.

$$\ln\left(p\tau_{\text{V-T}}\right) = A\left(T_{\text{T}}^{-1/3} - 0.015\mu^{1/4}\right) - 18.42 \tag{3.2}$$

For the $O_2 - O_2$ process, the reduced mass, μ, is 16 and the correlation factor, A, is 129 and for the $O_2 - Ar$ process, the reduced mass is 17.8 and the correlation factor

is 165. For mixtures of oxygen in argon, the relaxation time was calculated according to the mixing rule.

$$\frac{1}{\tau_{\text{V-T}}^{\text{mix}}} = \frac{X_{O_2}}{\tau_{\text{V-T}}^{O_2-O_2}} + \frac{1 - X_{O_2}}{\tau_{\text{V-T}}^{O_2-Ar}} \tag{3.3}$$

Ignoring relaxation, the test gas conditions in the shock tube can be understood by considering three regions. "Region 1" is the test gas at room temperature and initial pressure in the driven section before the shock arrives. The shock then travels through the test gas characterized by a jump in temperature and pressure leading to "Region 2." Once the shock reaches the end wall it reflects back causing an additional jump in temperature and pressure leading to "Region 5." However, as mentioned previously, while translational and rotational energy reach equilibrium within a few collisions, vibrational energy takes many collisions to reach equilibrium so vibrational relaxation must be taken into account.

The "x-t" diagram in Figure 3.2 shows the relaxation process at different locations and times in the shock tube. We will refer to this Figure to describe our in-house code and method for modeling the vibrational relaxation process. Immediately behind the incident shock, termed "F2", vibrational energy is frozen at the region 1 level but there is a jump in the translational and rotational energy, and hence temperature T_{T}. Across this incident shock, conservation of mass, momentum, and energy, along with the region 1 conditions and the incident shock speed, can be used to calculate the conditions at F2 as described in detail previously.[42] The conditions in the incident shock relaxation zone were determined by first calculating the vibrational energy by numerical solution of the Bethe-Teller Equation using the Euler method with a time step of 0.4 μs.

$$E_{\text{V}}(t + dt) = E_{\text{V}}(t) + dt \left[\frac{E_{\text{V}}^{*}\left(T_{\text{T}}\left(t\right)\right) - E_{\text{V}}\left(T_{\text{V}}\left(t\right)\right)}{\tau_{\text{V-T}}\left(T_{\text{T}}\left(t\right)\right)} \right] \tag{3.4}$$

The vibrational energy as a function of temperature was determined by subtracting the fully excited rotational and translational energy from the enthalpy obtained from the 7-coefficient NASA polynomials,[43] which allow computation of thermodynamic data within 0.5 percent error. Notice that since the relaxation time is also a function of the translational temperature, $\tau_{\text{V-T}}$ is not a constant during the relaxation process.

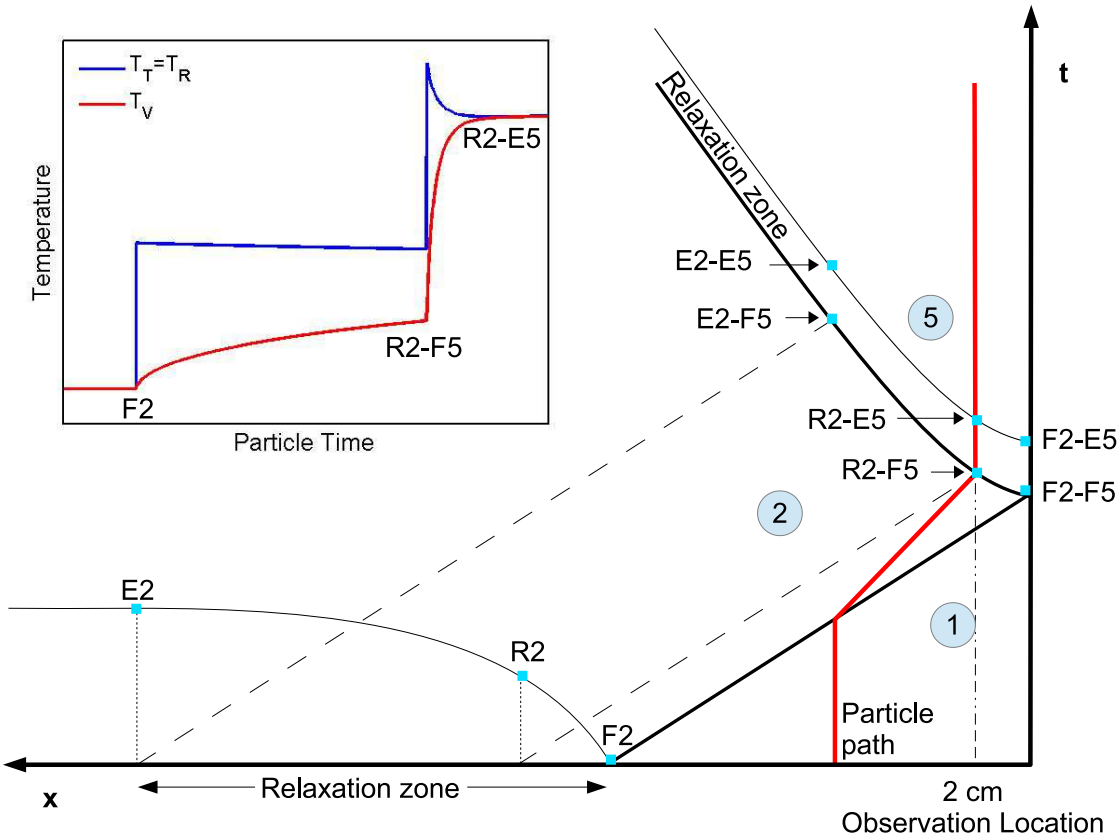

Figure 3.2: "x-t" diagram of an incident and reflected shock in a shock tube showing the relaxation zones. The inset shows representative translational (T_{T}), rotational (T_{R}), and vibrational (T_{V}) temperatures over time along the particle path.

Next, the same calculations used to determine the conditions at F2 were used to determine the conditions in the relaxation zone for this time step, except that the vibrational energy was adjusted to the value for the current time step. Over this time there is an increase in the vibrational temperature and a decrease in the translational and rotational temperatures due to the transfer of energy during relaxation. This process was then repeated for each additional time step until the vibrational and translational temperatures were equal and equilibrium was attained, termed "E2".

The reflected shock travels back through region 2, in most cases before equilibrium is reached. Therefore, the conditions in the relaxation zone must be determined for the time when the reflected shock passes the observation location. Since there is bulk flow of the gas behind the incident shock, the particle time in region 2 is different from the lab time between passage of the incident and reflected shocks. The particle time can be determined from the velocity of the gas in region 2, the velocities of the incident and reflected shocks, and the distance between the end wall and the observation location. Since the reflected shock velocity depends on the conditions into which it is traveling, an iterative approach was used to determine the particle time in region 2 and the partially relaxed conditions in region 2 at the observation location when the reflected shock reaches the observation location, termed "R2".

Immediately behind the reflected shock, termed "R2-F5", vibrational energy is again frozen at the R2 level but there is a jump in the translational and rotational energy. Strictly speaking, the reflected shock speed slows down a small amount as it moves through the relaxation zone of region 2 and the gas is not fully stagnated in the relaxation zone behind the reflected shock,[44] but to avoid solving for the conditions throughout region 5 with the 1-D unsteady flow equations, we have developed an approximate method. In our method, we use the conservation of mass, momentum, and energy across the reflected shock, along with the R2 conditions and the approximation that the reflected shock stagnates the gas, to calculate the conditions at R2-F5. This is justified because the energy of the gas associated with the mean motion is negligibly small[31] for dilute oxygen mixtures. Instead of using the conservation equations again to determine the conditions in the relaxation zone, which would be inconsistent with neglecting the mean motion of the gas, we have used a novel method that keeps track

of the small enthalpy change in the relaxation zone. Instead of making the constant enthalpy, constant pressure approximation, as has been used previously,[31] we use the measured pressure to calculate the enthalpy based on the relation

$$dh = vdp \tag{3.5}$$

that applies along a particle path. As a first approximation we also neglect motion of the relaxing gases in region 5, so that this equation applies at the fixed measurement location. Again, a numerical solution was used to determine the conditions in the relaxation zone. First, the vibrational energy was calculated for the first time step from the Bethe-Teller Equation, then the enthalpy and translational temperature were calculated by numerical solution of Equation 3.5 using the Euler method. This process was then repeated for each additional time step until the vibrational and translational temperatures were equal and equilibrium was attained, termed "R2-E5".

Using the absorption model,[10] the oxygen absorbance was calculated as a function of time during the relaxation behind the reflected shock from the conditions obtained from the relaxation model. This modeled absorbance was then compared to the measured absorbance. As mentioned above, initially the relaxation time used in this model was the time from the Millikan and White correlation. The modeled absorbance was then fit to the measured absorbance using a nonlinear least squares fitting algorithm by adjusting a multiplicative factor on the Millikan and White correlations. In this way, the temperature dependence of the relaxation time was maintained, meaning the relaxation time was allowed to change during the relaxation as a function of temperature, but it was scaled in such a way as to fit the measured absorbance. Figure 3.3 shows an example of a comparison between the measured absorbance and the modeled absorbance based on the Millikan and White and best-fit relaxation times. For this 2% O_2/Ar test gas the relaxation time from the Millikan and White correlation matches the measurement very well, within ±2%. The consistent, close agreement at all values of time provide some confirmation of the B-T SHO model in which a Boltzmnn distribution is maintained during relaxation.

For the undiluted oxygen measurements, the density change during relaxation

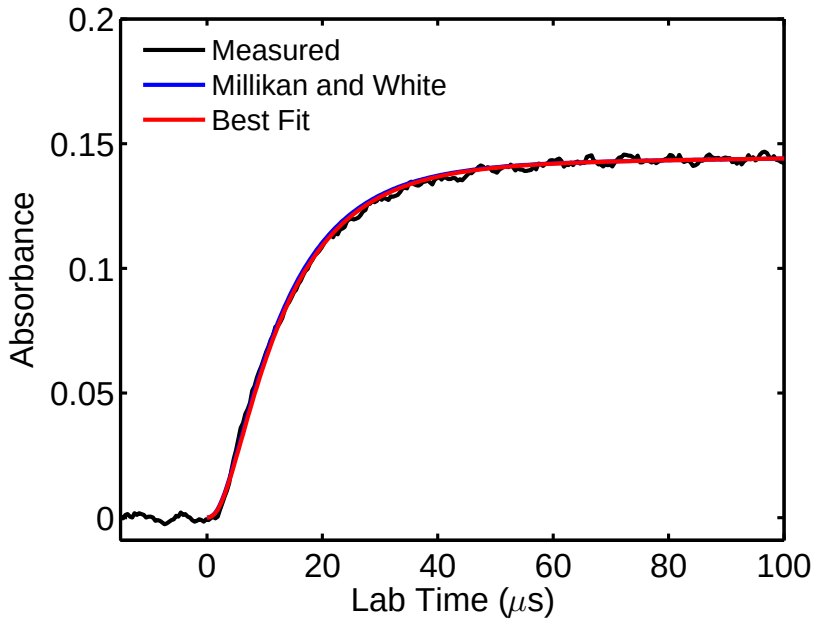

Figure 3.3: Comparison between measured absorbance at 211.2 nm behind a reflected shock wave for a 2% O_2/Ar test gas and modeled absorbance with relaxation times from the Millikan and White correlation[5] and the scaled time to best fit the measurement. Initial (R2-F5) conditions: $T_{\mathrm{T}} = 3033$ K, P = 0.46 atm, Millikan and White $\tau_{\text{V-T}} = 11.5$ μs, Best Fit $\tau_{\text{V-T}} = 11.7$ μs.

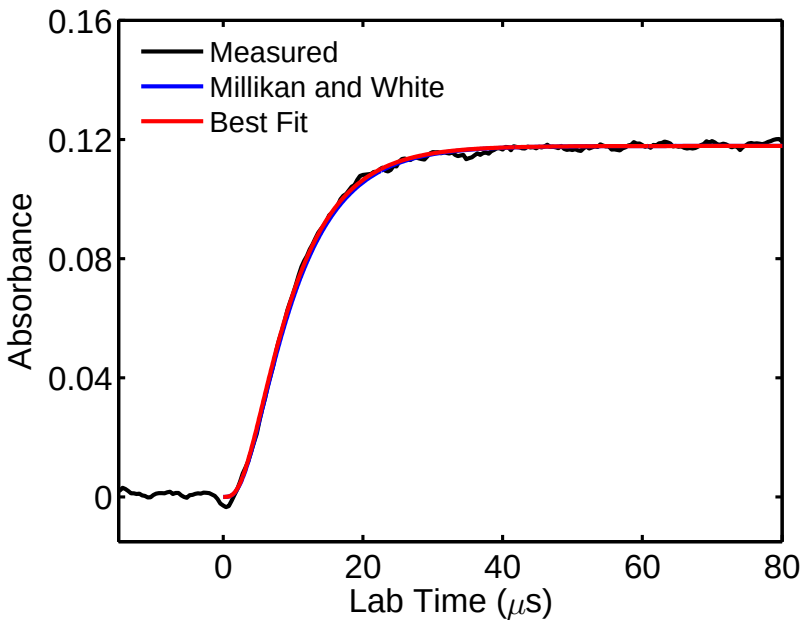

Figure 3.4: Comparison between measured absorbance at 223.1 nm behind an incident shock wave for an undiluted O_2 test gas and modeled absorbance with relaxation times from the Millikan and White correlation[5] and the scaled time to best fit the measurement. Initial (F2) conditions: $T_{\mathrm{T}} = 2235$ K, P = 0.12 atm, Millikan and White $\tau_{\mathrm{V\text{-}T}} = 33.3$ μs, Best Fit $\tau_{\mathrm{V\text{-}T}} = 32.5$ μs.

behind the reflected shock is significant enough such that we cannot retain the assumptions that the kinetic energy of the gas associated with the mean motion is negligibly small, and that motion of the gas can be ignored. Therefore, it would be necessary to solve for the conditions throughout region 5 with the 1-D unsteady flow equations. In the future, measurements of undiluted oxygen behind reflected shocks will be analyzed in this way. However, the present measurements of undiluted oxygen were limited to incident shocks. The analysis was performed in the same method as described above up until the determination of equilibrium after the incident shock. Figure 3.4 shows an example of a comparison between the measured absorbance and the modeled absorbance based on the Millikan and White and best-fit relaxation times, which again shows that the Millikan and White correlation matches the measurement very well, within ±2%.

3.3 Dissociation Model

The analysis of the experimental data was performed by kinetic modeling of the dissociation using the CHEMKIN-PRO software suite[45] to solve the energy equation from a starting vibrational-equilibrium temperature and composition and a prescribed pressure profile. The temperature behind the reflected shock was calculated using an in-house code which modified an existing frozen shock equation solver[42] to include the effects of vibrational relaxation, as described above. The vibrational relaxation time was calculated using the empirical correlation developed by Millikan and White,[5] which predicts values in good agreement with our current study. The dissociation was modeled assuming it was not coupled to the vibrational relaxation. The short time (typically 7 μs at 6000 K and 0.4 atm) for the vibrational temperature to approach within 3% of the translational temperature was considered as an incubation time for the dissociation calculation.

For many of the experiments, non-ideal effects in the shock tube flows led to an increase in pressure in the test region behind the reflected shock that was not due to the dissociation itself. In several experiments, this pressure rise was eliminated through the use of driver inserts.[46] In order to analyze all of the experiments, the pressure rise was included in the dissociation model by specifying the pressure as a function of time as an input to the CHEMKIN-PRO kinetic model. The kinetic mechanism used in this calculation included two reactions, listed in Table 3.1, with the initial dissociation rate coefficients taken from the model by Baulch et. al.[8] The dissociation due to collisions with atomic oxygen was not included because its effect was negligible in the early times during which the measurement was fit to determine the rate.

Table 3.1: Oxygen/Argon dissociation reactions with the dissociation rate coefficients taken from the model by Baulch et. al.[8]

Reaction	$k_d = AT^b \exp\left(\frac{-E_a}{RT}\right)$ cm^3/mol-s		
	A	b	E_a (kcal/mol)
$O_2 + Ar \rightleftharpoons O + O + Ar$	1.8×10^{18}	-1	117.93
$O_2 + O_2 \rightleftharpoons O + O + O_2$	9.8×10^{24}	-2.5	117.93

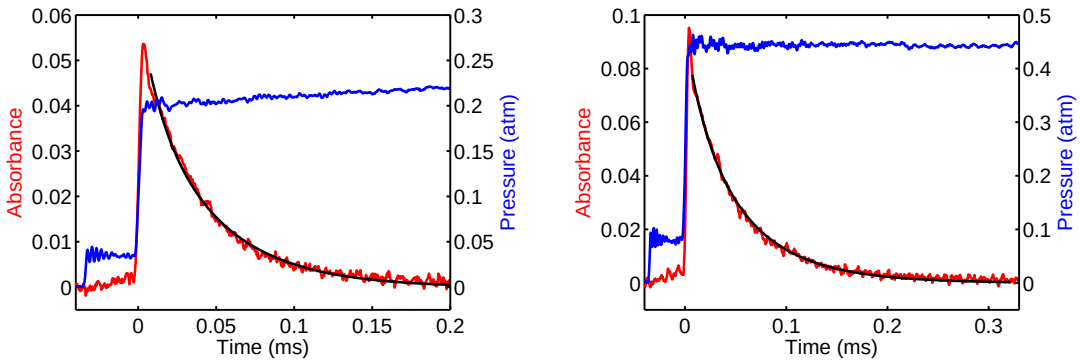

(a) (b)

Figure 3.5: Absorbance and pressure measurements for two sample experiments during dissociation of a mixture of 2% oxygen in argon along with the best fit modeled absorbance shown in black. (a) shows a case with a pressure rise that had an initial (vibrational-equilibrium) temperature of 6832 K and the absorbance was measured at 216 nm. (b) shows a case with near-constant pressure that had an initial (vibrational-equilibrium) temperature of 6006 K and the absorbance was measured at 215.35 nm.

Using the "Spectrum" absorption model,[10] the oxygen absorbance was calculated as a function of time during the dissociation behind the reflected shock from the measured pressure and calculated temperature and oxygen mole fraction. This modeled absorbance was then compared to the measured absorbance, and the rate coefficient of the argon reaction was adjusted by a multiplicative factor until the model matched the measurement. The mixtures were sufficiently dilute such that the rate of the dissociation due to oxygen did not significantly affect the measurement. Figure 3.5 shows two sample absorbance and pressure measurements, one with increasing pressure and one with near-constant pressure.

Chapter 4: Results

4.1 Vibrational Relaxation Experiments

The vibrational relaxation time of oxygen was measured over the translational/rotational temperature range of 1000 - 4000 K and pressures from 0.2 to 1 atm for mixtures of 2% O_2/Ar and 1000 - 3300 K and pressures from 0.05 to 0.7 atm for undiluted oxygen. As mentioned previously, the undiluted oxygen vibrational relaxation times were measured behind incident shocks, since the density change behind reflected shocks was non-negligible. Incident shocks have the advantage of being steady, and therefore simpler to analyze, however the drawbacks include a loss of time resolution due to the bulk fluid motion and higher burst pressures to achieve comparable temperatures to those generated behind reflected shocks. Most of the 2% O_2/Ar vibrational relaxation times were measured behind reflected shocks, but a few were measured behind incident shocks as a consistency check of the assumption of negligible density change.

Figure 4.1 shows the results of these measurements on a Landau-Teller plot. Our results are compared to the empirical correlations from Millikan and White[5] given by Equation 3.2 where the contribution from both oxygen and argon was accounted for using Equation 3.3 for the 2% O_2/Ar mixture. The rms deviation between our measurements and the emirical correlations were 5% and 8% for the undiluted oxygen and 2% O_2/Ar mixture, respectively. Also shown on the plot are the previous measurements used to develop these correlations including measurements by White and Millikan[1] and Losev and Generalov[3] for O_2-O_2 and by White and Millikan[2] and Camac[4] for O_2-Ar. The conditions and results for each measurement are also listed in Table 4.1.

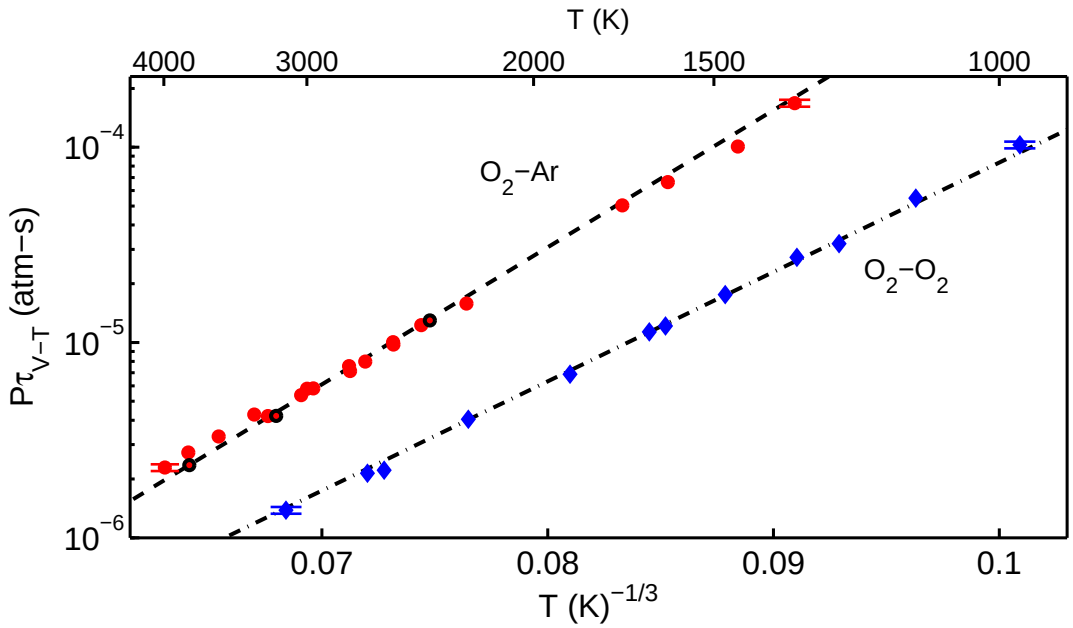

(a)

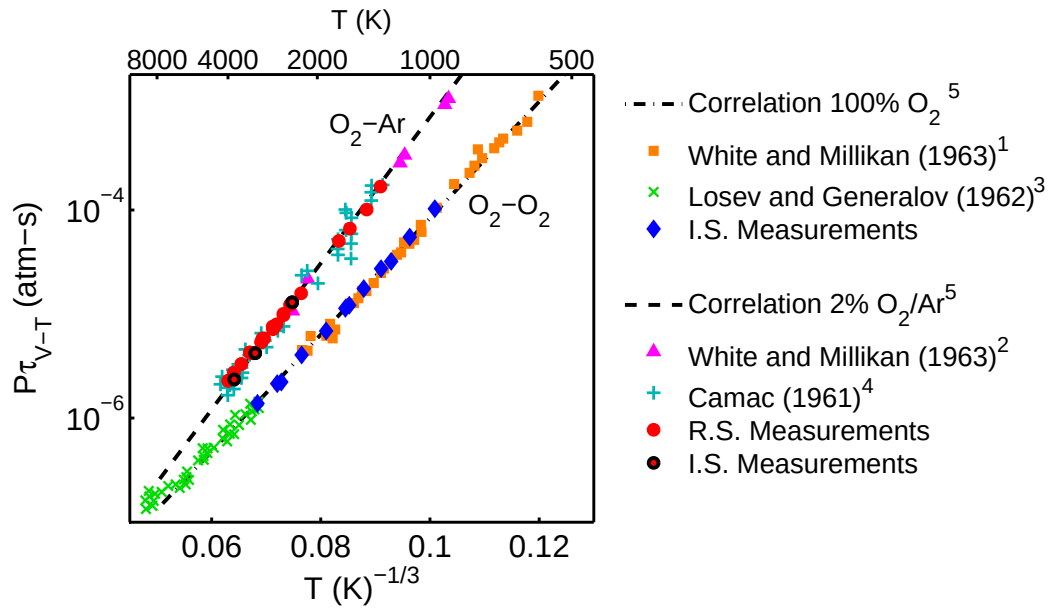

(b)

Figure 4.1: Vibrational relaxation times plotted on a Landau-Teller diagram. The vibrational relaxation time of oxygen was measured behind incident shocks (I.S.) and reflected shocks (R.S.) for undiluted oxygen and mixtures of 2% O_2/Ar. The measurements are compared to the empirical correlation given by Equations 3.2 and 3.3 and the previous experiments used to develop the correlation. (a) shows a close view of our data demonstrating the lower scatter of our measurements compared with previous experiments. (b) shows a broader temperature range to show all the previous experiments.

Table 4.1: The measurement initial conditions and results are listed for the 2% O_2/Ar mixtures studied behind reflected shock waves (* indicates incident shocks) and the undiluted O_2 studied behind incident shock waves.

2% O_2/Ar			**Undiluted O_2**		
$T_{T,i}$ (K)	P_i (atm)	τ_{V-T} (μs)	$T_{T,i}$ (K)	P_i (atm)	τ_{V-T} (μs)
1330	0.16	77.9	973	0.68	151.9
1447	2.13	47.3	1120	0.53	103.4
1610	2.08	31.9	1247	0.31	101.8
1730	1.90	26.5	1325	0.40	68.0
2242	0.88	18.0	1474	0.24	73.9
*2392	0.36	35.8	1616	0.19	65.0
2428	0.71	17.4	1658	0.09	123.9
2553	0.80	12.2	1883	0.06	107.2
2555	0.79	12.7	2235	0.12	34.2
2688	0.74	10.8	2597	0.07	33.5
2765	0.65	11.0	2678	0.06	34.0
2770	0.55	13.8	3124	0.05	26.4
2964	0.70	8.3			
2999	0.47	12.4			
3033	0.46	11.7			
*3184	0.20	21.1			
3236	0.65	6.4			
3325	0.37	11.7			
3570	0.28	11.9			
*3792	0.11	20.9			
3800	0.22	12.2			
3991	0.19	12.3			

Our current measurements have much lower scatter than the previous measurements and demonstrate the improved performance possible with the use of laser absorption spectroscopy. A variety of sources of measurement uncertainty exist and careful attention was paid to each one in order to minimize the overall uncertainty. In particular, the incident shock velocity was measured over the last 1.5 m of the shock tube with attenuation less than 1% and a maximum scatter of 0.5%. This led to accurate calculations of the gas temperature behind the incident and reflected shocks within ±1%. The pressure was measured with an uncertainty less than ±2.5% and as mentioned above, any small changes in pressure were also accounted for in the relaxation model. The calculated pressure was also in agreement with the measured pressure. As discussed previously, the laser linewidth was between 0.07 - 0.18 nm, but our analysis shows that the resulting vibrational relaxation times determined when using absorption models with each of these values for the FWHM differ by only 0.5%. Another source of uncertainty came from determining time zero. Time zero was initially defined based on the pressure rise, but since it is not instantaneous the time zero was adjusted to minimize the residual between the measurement and the fit. There was little change in the residual over a time range of 0.3 μs which led to an uncertainty in the relaxation time of ±2.3%. The last source of uncertainty came from the fit of the model to the measurement which resulted in an uncertainty in the relaxation time of ±2%. Figure 4.2 shows the contribution of each of these sources of uncertainty on the product of the pressure and the relaxation time. The overall uncertainty from each of these individual sources was ±4%.

The absorption near 211 nm was measured to study the 2% O_2/Ar mixture; the absorption at this wavelength was due primarily to $v'' = 4$. To prevent saturation, in the undiluted oxygen experiments we utilized the weaker absorption near 223 nm, which is due primarily to $v'' = 5$. The same vibrational relaxation times were recovered from additional experiments performed in a 4% O_2/Ar mixture at both wavelengths. This, along with the agreement between our measurements and previous experiments, which were likely measuring other vibrational levels, supports the use of B-T modeling and suggests that there is a well-defined vibrational temperature throughout the relaxation process.

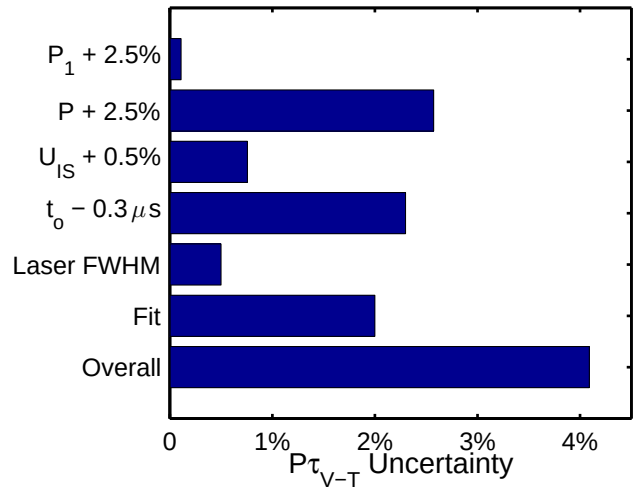

Figure 4.2: The effects of uncertainty in the pressure, incident shock speed, time zero, laser linewidth, and best fit on the measured value of $P\tau_{\text{V-T}}$ along with the overall uncertainty.

Since these measurements agree within our uncertainty with the empirical correlation from Millikan and White,[5] we recommend no change. However, our low-scatter, laser-based measurements justify a reduction in the uncertainty of $\tau_{\text{V-T}}$ for oxygen for temperatures between 1000 - 4000 K, as may prove useful in evaluation or refinement of theoretical models for $\tau_{\text{V-T}}$ in oxygen and oxygen/argon mixtures.

4.2 Dissociation Experiments

The dissociation rate coefficient, k_d, for the dissociation reaction $O_2 + Ar \rightleftharpoons O + O + Ar$ was measured for mixtures of 2% O_2 in Ar for temperatures between 4400 - 7900 K and pressures from 0.2 to 1 atm. The absorption near 216 nm was chosen for these measurements because it coincided with the highest output power from the laser, which was necessary in order to eliminate the effects of emission. The absorption at this wavelength was due primarily to vibrational levels $v'' = 4$ and $v'' = 5$.

Figure 4.3 shows the results of these measurements on an Arrhenius plot. Our measurements are compared to the models from Camac and Vaughan[6] and Baulch

et. al.[8] as well as the previous measurements by Shexnayder and Evans,[11] Camac and Vaughan,[6] Breshears et. al.[12] Wray,[13] and the more recent work by Ibraguimova et. al.[14]

Our results are in better agreement with the model and experiments by Camac and Vaughan[6] than the other model and experiments. Table 4.2 lists the numeric values for the measured dissociation rate coefficient at each initial equilibrium temperature and pressure along with the percent change in the pressure during the time for 99% dissociation. A best-fit expression for the current data is given by $k_d = 2.87 \times 10^{18} T^{-1} \exp\left(^{-58580K}/_{T}\right)$ ($\pm 7\%$) cm^3/mol-s. The activation energy measured is in excellent agreement (1.4%) with the earlier studies.

Our current measurements have much lower scatter than the previous measurements and demonstrate the improved performance possible with the use of laser absorption spectroscopy. A variety of sources of measurement uncertainty exist and careful attention was paid to each one in order to minimize the overall uncertainty. In particular, the incident shock velocity was measured over the last 1.5 m of the shock tube with attenuation less than 1% and a maximum scatter of 0.5%. This led to accurate calculations of the gas temperature behind the incident and reflected shocks within $\pm 1\%$. The pressure was measured with an uncertainty less than $\pm 2.5\%$ and as mentioned above, any changes in pressure were also accounted for in the dissociation model. The calculated pressure was also in agreement with the initial measured pressure. The largest uncertainty came from fitting the model to the measured absorbance which was typically $\pm 5\%$. Combining the various sources of uncertainty yield an uncertainty in the measured dissociation rate coefficient of $\pm 7\%$.

The consistency between the measurements with near-constant pressure and the measurements with increasing pressure demonstrate that this pressure rise does not noticeably affect the results. There are three effects in play that affect the pressure in the test gas: 1) negative dP/dt because of cooling by dissociation, 2) positive dP/dt due to shock tube boundary layer and attenuation effects, and finally, 3) positive dP/dt effects by the fact that the shock tube is not a constant volume reactor and it will try to achieve a uniform pressure behind the reflected shock (somewhere between the pressure caused by the drop from the dissociation and the pressure immediately

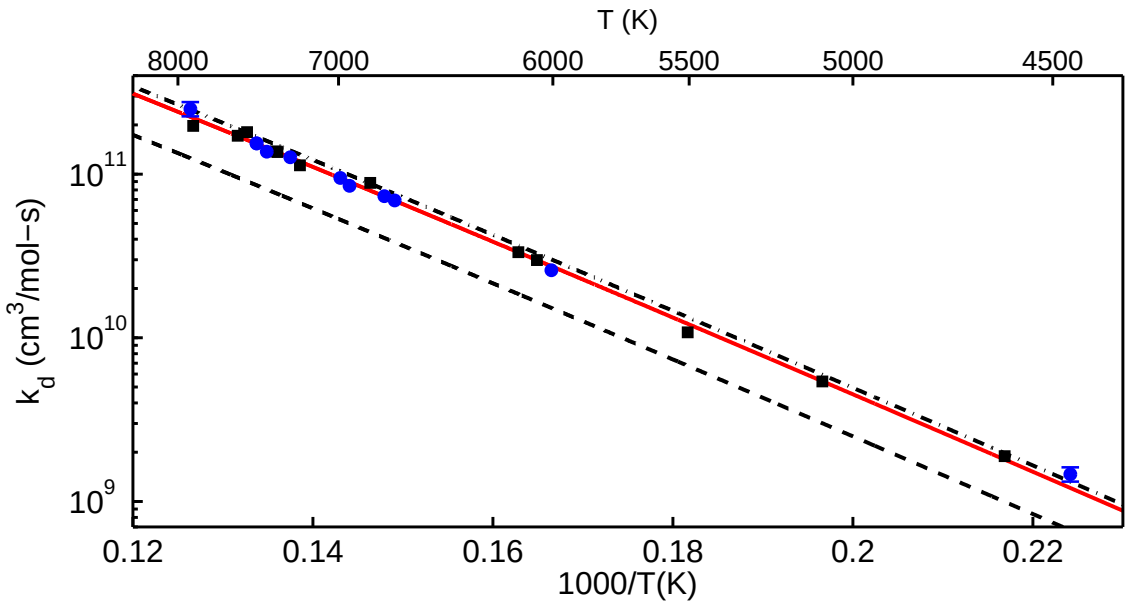

(a)

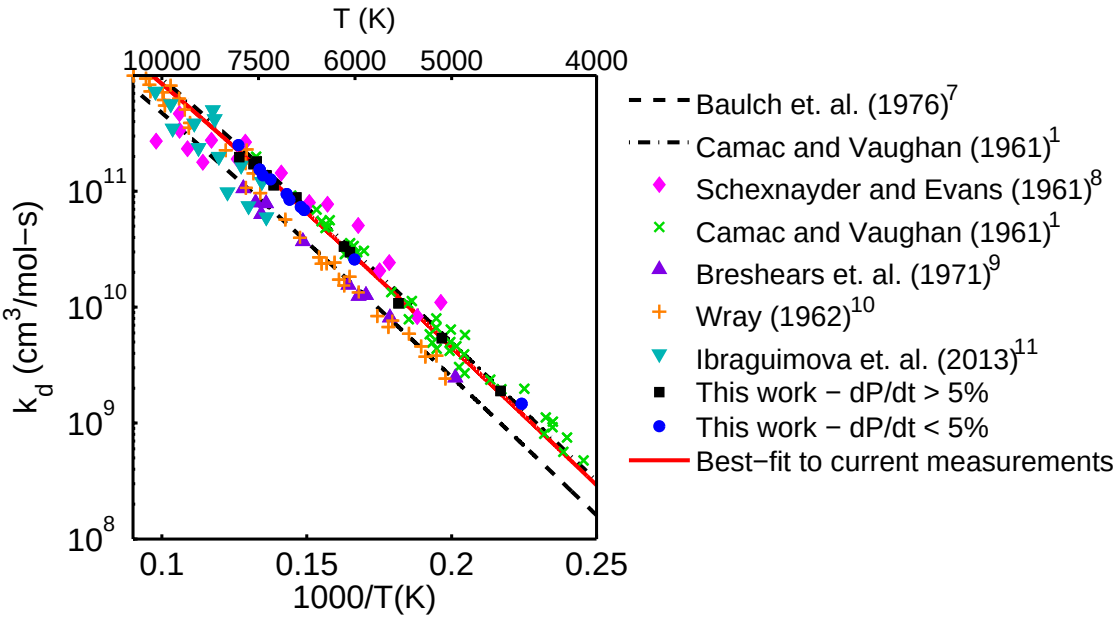

(b)

Figure 4.3: Values of the dissociation rate coefficient, k_d, for the dissociation reaction $O_2 + Ar \rightleftharpoons O + O + Ar$ measured for mixtures of 2% O_2 in Ar compared to previously published models[6,8] and experiments.[6,11–14] dP/dt is defined here as the percent change in the pressure during the time for 99% dissociation. (a) shows a close view of our data demonstrating the lower scatter of our measurements compared with previous experiments. (b) shows a broader temperature range to show all the previous experiments.

Table 4.2: Values of the dissociation rate coefficient, k_d, for the dissociation reaction $O_2 + Ar \rightleftharpoons O + O + Ar$ measured for mixtures of 2% O_2 in Ar at each initial equilibrium temperature and pressure along with the dP/dt, defined here as the percent change in the pressure during the time for 99% dissociation.

$\mathbf{T_{eq}}$ **(K)**	$\mathbf{P_i}$ **(atm)**	**dP/dt (%)**	$\boldsymbol{k_d}$ $(\boldsymbol{cm^3/mol \cdot s})$
4461	0.95	3.8%	1.47×10^{9}
4611	0.81	10.9%	1.89×10^{9}
5086	0.66	14.2%	5.41×10^{9}
5505	0.39	14.9%	1.08×10^{10}
6006	0.44	-0.5%	2.59×10^{10}
6064	0.51	5.0%	2.98×10^{10}
6141	0.26	10.8%	3.33×10^{10}
6707	0.35	2.0%	6.51×10^{10}
6759	0.29	4.5%	7.33×10^{10}
6832	0.20	11.0%	8.85×10^{10}
6941	0.51	4.6%	8.49×10^{10}
6990	0.60	4.5%	9.47×10^{10}
7217	0.30	4.3%	1.13×10^{11}
7273	0.25	4.1%	1.27×10^{11}
7349	0.40	6.1%	1.36×10^{11}
7359	0.25	5.4%	1.38×10^{11}
7414	0.25	4.7%	1.37×10^{11}
7476	0.26	4.7%	1.54×10^{11}
7478	0.25	4.3%	1.54×10^{11}
7536	0.25	5.3%	1.81×10^{11}
7596	0.25	6.3%	1.72×10^{11}
7892	0.33	6.1%	1.97×10^{11}
7912	0.60	1.6%	2.50×10^{11}

behind the reflected shock wave as it moves away from the end wall). The pressure rise for the measurements was always less than 15%, so at least while a pressure change is within this deviation the results are still valid as long as the pressure rise is included in the model. This eliminates the necessity to use driver inserts to maintain a constant pressure during dissociation, which require numerous repeated shocks in order to design the proper insert for the each specific test condition.

Chapter 5: Summary and Future Work

5.1 Summary of Current Results

Laser absorption spectroscopy was used to measure vibrational relaxation and dissociation of oxygen in a shock tube. An absorption model for the bound-bound transitions in the Schumann-Runge system of oxygen was developed to study the temperature dependence of the absorption and select vibrational level dependent wavelengths, however, an absorption model developed previously[10] was used for the analysis since it inlcuded both bound-bound and bound-unbound transitions.

The vibrational relaxation of undiluted oxygen was studied behind incident shocks at initial post-shock translational/rotational temperatures from 1000 - 3300 K and pressures from 0.05 to 0.7 atm while a mixture of 2% oxygen in argon was studied behind incident and reflected shocks at initial translational/rotational temperatures from 1000 - 4000 K and pressures from 0.2 to 1 atm. The overall uncertainty for these measurements was ±4%. Our measurements were in agreement with the empirical correlation from Millikan and White,[5] with lower scatter than the previous experiments. Our low-scatter, laser-based measurements justify a reduction in the uncertainty of $\tau_{\text{V-T}}$ for oxygen for temperatures between 1000 - 4000 K, as may prove useful in evaluation or refinement of theoretical models for $\tau_{\text{V-T}}$ in oxygen and oxygen/argon mixtures.

The dissociation rate coefficient for oxygen in argon, $O_2 + Ar \rightleftharpoons O + O + Ar$, was studied using mixtures of 2% oxygen in argon behind reflected shocks at initial equilibirum temperatures from 4400 - 7900 K and pressures from 0.2 to 1 atm. The overall uncertainty for these measurements was ±7%. A best-fit experession for

the current data is given by $k_d = 2.87 \times 10^{18} T^{-1} \exp\left(^{-58580K}/_{T}\right)$ ($\pm 5\%$) cm^3/mol-s. The activation energy measured is in excellent agreement (1.4%) with the earlier studies. The consistency between the measurements with near constant pressure and the measurements with increasing pressure demonstrate that this pressure rise does not noticeably affect the results as long as it is included in the model.

5.2 Future Work

Future work is planned in all of the areas studied in this work including improvement of the absorption model and additional vibrational relaxation and dissociation experiments. We are continuing our collaboration with the authors of the Spectrum model to use our narrower linewidth laser measurements to refine the wavelength dependence of their model. A shock wave model which solves for the conditions throughout region 5 with the 1-D unsteady flow equations is being developed by our collaborators at the University of Michigan, which will be used to study the vibrational relaxation of undiluted oxygen behind reflected shock waves, since these experiments were not able to be analyzed with our model neglecting the mean motion of the gas. Additional mixtures will also be measured to study the vibrational relaxation of oxygen and nitrogen in air species. Lastly, additional dissociation experiments will expand these measurements to study other reactions involved in high temperature air chemistry relevant to hypersonic vehicles. The current work and this planned future work aims to provide modern, low-scatter measurements to aid in the evaluation and refinement of theoretical models for the vibrational relaxation and dissociation involved in the thermochemical nonequilibrium processes relevant to hypersonic vehicles.

Bibliography

[1] D. R. White and R. C. Millikan, "Vibrational relaxation of oxygen," *The Journal of Chemical Physics*, vol. 39, pp. 1803–1806, 1963.

[2] ——, "Oxygen vibrational relaxation in O_2-He and O_2-Ar mixtures," *The Journal of Chemical Physics*, vol. 39, pp. 1807–1808, 1963.

[3] S. A. Losev and N. A. Generalov, "A study of the excitation of vibrations and dissociation of oxygen molecules at high temperatures," in *Soviet Physics Doklady*, vol. 6, 1962, p. 1081.

[4] M. Camac, "O_2 vibration relaxation in oxygen-argon mixtures," *The Journal of Chemical Physics*, vol. 34, no. 2, pp. 448–459, 1961.

[5] R. C. Millikan and D. R. White, "Systematics of vibrational relaxation," *The Journal of chemical physics*, vol. 39, pp. 3209–3213, 1963.

[6] M. Camac and A. Vaughan, "O_2 dissociation rates in O_2-Ar mixtures," *The Journal of Chemical Physics*, vol. 34, no. 2, pp. 460–470, 1961.

[7] J. B. Tatum and J. K. G. Watson, "Rotational line strengths in $^3\Sigma^{\pm} -^3 \Sigma^{\pm}$ transitions with intermediate coupling," *Canadian Journal of Physics*, vol. 49, no. 21, pp. 2693–2703, 1971.

[8] D. L. Baulch, D. G. Drysdale, D. G. Horne, and A. C. Lloyd, "Evaluated kinetic data for high-temperature reactions. volume 1. homogeneous gas phase reactions of the H_2-O_2 system," *Journal of physical and chemical reference data*, vol. 15, no. 2, pp. 465–592, 1972.

[9] P. H. Krupenie, "The spectrum of molecular oxygen," *Journal of Physical and Chemical Reference Data*, vol. 1, pp. 423–534, 1972.

[10] N. G. Bykova and L. A. Kuznetsova, "Study of the absorption characteristics of molecular oxygen in the Schumann-Runge system at high temperatures: I. Calculations of absorption spectra," *Optics and Spectroscopy*, vol. 105, no. 5, pp. 668–673, 2008.

[11] C. J. Schexnayder Jr and J. S. Evans, "Measurements of the dissociation rate of molecular oxygen," National Aeronautics and Space Administration. Langley Research Center, Langley Field, Va., Tech. Rep., 1961.

[12] W. D. Breshears, P. F. Bird, and J. H. Kiefer, "Density gradient measurements of O_2 dissociation in shock waves," *The Journal of Chemical Physics*, vol. 55, no. 8, pp. 4017–4026, 1971.

[13] K. L. Wray, "Shock-tube study of the coupling of the O_2–ar rates of dissociation and vibrational relaxation," *The Journal of Chemical Physics*, vol. 37, no. 6, pp. 1254–1263, 1962.

[14] L. B. Ibraguimova, A. L. Sergievskaya, V. Y. Levashov, O. P. Shatalov, Y. V. Tunik, and I. E. Zabelinskii, "Investigation of oxygen dissociation and vibrational relaxation at temperatures 4000–10 800 k," *The Journal of chemical physics*, vol. 139, no. 3, p. 034317, 2013.

[15] J. M. Hank, J. S. Murphy, and R. C. Mutzman, "The X-51A scramjet engine flight demonstration program," *AIAA Paper*, vol. 2008-2540, 2008.

[16] S. H. Walker, J. Sherk, D. Shell, R. Schena, J. Bergmann, and J. Gladbach, "The DARPA/AF falcon program: The hypersonic technology vehicle #2 (HTV-2) flight demonstration phase," *AIAA Paper*, vol. 2008-2539, 2008.

[17] M. D. J. Dolvin, "Hypersonic international flight research and experimentation," in *16th AIAA/DLR/DGLR International Space Planes and Hypersonic Systems and Technologies Conference. Bremen, Germany: AIAA*, vol. 2009-7228, 2009.

[18] R. L. Kimmel and D. Adamczak, "HIFiRE-1 background and lessons learned," *AIAA Paper*, vol. 2012-1088, 2012.

[19] A. Martin, L. C. Scalabrin, and I. D. Boyd, "High performance modeling of atmospheric re-entry vehicles," in *Journal of Physics: Conference Series*, vol. 341, no. 012002. IOP Publishing, 2012.

[20] C. Park, "Review of chemical-kinetic problems of future NASA missions. I-Earth entries," *Journal of Thermophysics and Heat Transfer*, vol. 7, no. 3, pp. 385–398, 1993.

[21] V. H. Blackman, "Vibrational relaxation in oxygen and nitrogen," *Cambridge Univ Press*, 1955.

[22] H. A. Bethe and E. Teller, *Deviations from Thermal Equilibrium in Shock Waves*, ch. 14, pp. 295–345.

[23] J. F. Clarke and M. McChesney, *The dynamics of real gases.* Butterworths London, 1964, vol. 175.

[24] D. R. White and R. C. Millikan, "Oxygen vibrational relaxation in O_2-H_2 mixtures," *The Journal of Chemical Physics*, vol. 39, no. 8, pp. 2107–2108, 1963.

[25] R. C. Millikan and D. R. White, "Vibrational energy exchange between N_2 and CO. The vibrational relaxation of nitrogen," *The Journal of Chemical Physics*, vol. 39, pp. 98–101, 1963.

[26] D. R. White and R. C. Millikan, *Vibrational relaxation in air*, 1964, vol. 2.

[27] R. K. Hanson and W. Flower, "Verification of a simple relationship for shock-wave reflection in a relaxing gas," *AIAA Journal*, vol. 11, no. 12, pp. 1777–1778, 1973.

[28] R. K. Hanson and D. Baganoff, "Shock-tube study of vibrational relaxation in nitrogen using pressure measurements," *The Journal of Chemical Physics*, vol. 53, no. 11, pp. 4401–4403, 1970.

[29] R. K. Hanson, "Shock-tube study of vibrational relaxation in carbon monoxide using pressure measurements," *AIAA Journal*, vol. 9, no. 9, pp. 1811–1819, 1971.

[30] R. K. Hanson and D. Baganoff, "Shock-tube study of nitrogen dissociation rates using pressure measurements," *AIAA Journal*, vol. 10, no. 2, pp. 211–215, 1972.

[31] J. Appleton, "Shock-tube study of the vibrational relaxation of nitrogen using vacuum-ultraviolet light absorption," *The Journal of Chemical Physics*, vol. 47, pp. 3231–3240, 1967.

[32] G. Herzberg, *Molecular Spectra and Molecular Structure*, 2nd ed. Malabar, Fl: Krieger Publishing Company, 1950, vol. 1. Spectra of Diatomic Molecules.

[33] M. P. Lee and R. K. Hanson, "Calculations of o¡ sub¿ 2¡/sub¿ absorption and fluorescence at elevated temperatures for a broadband argonfluoride laser source at 193 nm," *Journal of Quantitative Spectroscopy and Radiative Transfer*, vol. 36, no. 5, pp. 425–440, 1986.

[34] D. M. Creek and R. W. Nicholls, "A comprehensive re-analysis of the O_2 $\left(B^3\Sigma_u^- - X^3\Sigma_g^-\right)$ Schumann-Runge band system," *Proceedings of the Royal Society of London. A. Mathematical and Physical Sciences*, vol. 341, no. 1627, pp. 517–536, 1975.

[35] A. J. Blake, "An atmospheric absorption model for the Schumann-Runge bands of oxygen," *Journal of Geophysical Research: Space Physics (1978–2012)*, vol. 84, no. A7, pp. 3272–3282, 1979.

[36] A. C. Allison, A. Dalgarno, and N. W. Pasachoff, "Absorption by vibrationally excited molecular oxygen in the Schumann-Runge continuum," *Planetary and Space Science*, vol. 19, no. 11, pp. 1463–1473, 1971.

[37] M. W. P. Cann, J. B. Shin, and R. W. Nicholls, "Oxygen absorption in the spectral range 180-300 nm for temperatures to 3000 k and pressures to 50 atm." *Canadian journal of physics*, vol. 62, no. 12, pp. 1738–1751, 1984.

[38] T. Walther, M. P. Larsen, and E. S. Fry, "Generation of Fourier-transform-limited 35-ns pulses with a ramp-hold-fire seeding technique in a Ti:sapphire laser," *Applied optics*, vol. 40, no. 18, pp. 3046–3050, 2001.

[39] R. Seiler, T. Paul, M. Andrist, and F. Merkt, "Generation of programmable near-Fourier-transform-limited pulses of narrow-band laser radiation from the near infrared to the vacuum ultraviolet," *Review of scientific instruments*, vol. 76, no. 10, p. 103103, 2005.

[40] M. Nishida, "Shock tubes," in *Handbook of Shock Waves, Three Volume Set*, G. Ben-Dor, O. Igra, and T. Elperin, Eds. Academic Press, 2001, vol. 1, pp. 553–585.

[41] Z. Hong, K.-Y. Lam, D. F. Davidson, and R. K. Hanson, "Broad-linewidth laser absorption measurements of oxygen between 211 and 235nm at high temperatures," *Journal of Quantitative Spectroscopy and Radiative Transfer*, vol. 112, no. 17, pp. 2698–2703, 2011.

[42] D. F. Davidson, "RGFROSH: a real gas frozen shock equation solver," Mechanical Engineering Department, Stanford University, Stanford (Ca, 94305), Tech. Rep. 1995-001-1.00, 1995.

[43] A. Burcat and B. Ruscic, "Third millenium ideal gas and condensed phase thermochemical database for combustion with updates from active thermochemical tables," Argonne National Laboratory and Technion Israel Institute of Technology, Tech. Rep. ANL-05/20 TAE 960, 1995.

[44] N. H. Johannesen, G. A. Bird, and H. K. Zienkiewicz, "Theoretical and experimental investigations of the reflexion of normal shock waves with vibrational relaxation," *J. Fluid Mech*, vol. 30, no. part 1, pp. 51–64, 1967.

[45] CHEMKIN-PRO, Reaction Design, Inc. San Diego, CA, Release 15101, 2010.

[46] Z. Hong, G. A. Pang, S. S. Vasu, D. F. Davidson, and R. K. Hanson, "The use of driver inserts to reduce non-ideal pressure variations behind reflected shock waves," *Shock Waves*, vol. 19, no. 2, pp. 113–123, 2009.